THE CASSINI ULTRAVIOLET IMAGING SPECTROGRAPH INVESTIGATION

LARRY W. ESPOSITO[1,*], CHARLES A. BARTH[1], JOSHUA E. COLWELL[1], GEORGE M. LAWRENCE[1], WILLIAM E. McCLINTOCK[1], A. IAN F. STEWART[1], H. UWE KELLER[2], AXEL KORTH[2], HANS LAUCHE[2], MICHEL C. FESTOU[3], ARTHUR L. LANE[4], CANDICE J. HANSEN[4], JUSTIN N. MAKI[4], ROBERT A. WEST[4], HERBERT JAHN[5], RALF REULKE[5], KERSTIN WARLICH[5], DONALD E. SHEMANSKY[6] and YUK L. YUNG[7]

[1] *University of Colorado, Laboratory for Atmospheric and Space Physics, 1234 Innovation Drive, Boulder, CO 80303, U.S.A.*

[2] *Max-Planck-Institut für Aeronomie, Max-Planck-Strasse 2, 37191 Katlenburg-Lindau, Germany*

[3] *Observatoire Midi-Pyrénées, 14 avenue E. Belin, F31400 Toulouse, France*

[4] *Jet Propulsion Laboratory, 4800 Oak Grove Drive, Pasadena, CA 91109, U.S.A.*

[5] *Deutsches Zentrum für Luft und Raumfahrt, Institut für Weltraumsensorik und Planetenerkundung, Rutherford Strasse 2, 12489 Berlin, Germany*

[6] *University of Southern California, Department of Aerospace Engineering, 854 W. 36th Place, Los Angeles, CA 90089, U.S.A.*

[7] *California Institute of Technology, Division of Geological and Planetary Sciences, MS 150-21, Pasadena, CA 91125, U.S.A.*

([*]Author for correspondence: E-mail: larry.esposito@lasp.colorado.edu)

(Received 8 July 1999; Accepted in final form 18 October 2000)

Abstract. The Cassini Ultraviolet Imaging Spectrograph (UVIS) is part of the remote sensing payload of the Cassini orbiter spacecraft. UVIS has two spectrographic channels that provide images and spectra covering the ranges from 56 to 118 nm and 110 to 190 nm. A third optical path with a solar blind CsI photocathode is used for high signal-to-noise-ratio stellar occultations by rings and atmospheres. A separate Hydrogen Deuterium Absorption Cell measures the relative abundance of deuterium and hydrogen from their Lyman-α emission. The UVIS science objectives include investigation of the chemistry, aerosols, clouds, and energy balance of the Titan and Saturn atmospheres; neutrals in the Saturn magnetosphere; the deuterium-to-hydrogen (D/H) ratio for Titan and Saturn; icy satellite surface properties; and the structure and evolution of Saturn's rings.

Keywords: Cassini, rings, Saturn, spectroscopy on Titan and on Saturn

Nomenclature

CASPER	Cassini Sequence Planner
CDS	Command and Data Handling Subsystem
CEM	Channel Electron Multiplier
CIRS	Composite Infrared Spectrometer
CODACON	Coded Anode Array Converter (see Lawrence and McClintock, 1996)
D/H	Deuterium/hydrogen (ratio)
DISR	Descent Imager/Spectral Radiometer
EUV	Extreme ultraviolet
EUVE	Extreme Ultraviolet Explorer
FOV	Field of view

Space Science Reviews **115:** 299–361, 2004.

FUV	Far ultraviolet
HDAC	Hydrogen-Deuterium Absorption Cell
HSP	High Speed Photometer
HST	Hubble Space Telescope
HUT	Hopkins Ultraviolet Telescope
HV	High voltage
HVPS	High Voltage Power Supply
IR	Infrared
IRIS	Infrared Interferometer Spectrometer
ISM	Interstellar medium
ISO	Infrared Science Observatory
ISS	Imaging Science Subsystem
IUE	International Ultraviolet Explorer
LISM	Local interstellar medium
MAPS	Magnetosphere and plasma science
MPAe	Max-Planck-Institut für Aeronomie
NIST	National Institute for Standards and Technology
PAD	Pulse Amplifier Discriminator
PPS	Voyager Photo-Polarimeter Subsystem
RTG	Radioisotope Thermoelectric Generator
RSP	Remote Sensing Platform
SIRTF	Space Infrared Telescope Facility
SMOW	Standard mean ocean water
SOHO	Solar and Heliospheric Observatory
SSR	Solid state recorders
STIS	Space Telescope Imaging Spectrometer
UV	Ultraviolet
UVIS	Ultraviolet Imaging Spectrograph
UVS	Voyager or Galileo Ultraviolet Spectrometer
VIMS	Visual and Infrared Mapping Spectrometer
WFPC2	Wide Field and Planetary Camera 2

1. Introduction

As part of the Cassini orbiter remote sensing payload, the Ultraviolet Imaging Spectrograph (UVIS) is coaligned with the cameras (ISS) and the infrared spectrometers (CIRS and VIMS; see their chapters in this volume). The spectrograph design draws on the University of Colorado experience of building UV spectrometers for the Mariner, Pioneer, and Galileo missions and extends the previous capabilities by using two-dimensional CODACON detectors and adding separate channels for high speed photometry and for measuring the deuterium-to-hydrogen ratio with a Hydrogen Deuterium Absorption Cell. The spectrographic channels cover the wavelength range from 56 to 190 nm. A special pickoff mirror allows solar occultation observations in the extreme UV. All parts of the experiment are housed in a rectangular case that is rigidly attached to the spacecraft's Remote Sensing

Platform (RSP). The instrument has its own microprocessor for storing and executing commands, and a limited memory to buffer and store observational data. Sequences of commands in the instrument memory are initiated by 'trigger' commands from the spacecraft's Command and Data Handling Subsystem (CDS). The UVIS microprocessor compresses, formats, and packetizes data for pickup and storage in the spacecraft's solid-state recorders (SSR) before eventual telemetry to Earth.

1.1. UVIS OBSERVATIONS

The Cassini orbital tour of Saturn consists of more than 70 orbits of Saturn and 44 close passes to Titan (see chapter by Wolf in Vol. 1). Each orbit of Saturn contains a number of phases: apoapsis, Titan flyby, Saturn periapse, and possible icy satellite flybys. Table I shows the planned UVIS observations in each of these phases. Detailed descriptions of each observation can be found in the internal document, *UVIS Observation Description Handbook* (ODH), latest revision 6/99, available from the Principal Investigator.

1.2. UVIS ANTICIPATED RESULTS

We include in this introduction a brief summary of anticipated results. More details can be found in the body of our chapter.

1.2.1. *Titan*

(1) *Atmospheric abundances*. UVIS will determine the altitudinal and latitudinal distribution and mixing ratios of CH_4, C_2H_6, and C_2H_2 via the detection of well-defined absorption features. Vertical profiles of these molecules will be determined from limb observations and solar and stellar occultations. Solar and stellar occultations will yield measurements of H, and H_2 as well as N, N_2, C_2H_4, C_4H_2, Ar, CO, and C_2N_2. The deuterium/hydrogen ratio will be determined. It may be possible to differentiate argon from nitrogen with UVIS in its high spectral resolution mode.

(2) *Atmospheric chemistry and distribution of species; aerosols*. Horizontal and vertical distribution of active species will be detected. The photochemistry of the atmosphere of Titan displays a rich interaction between hydrocarbons, oxygen, and nitrogen species. The overall chemical composition can be understood in terms of a small number of chemical cycles that generate more complex compounds from the simple parent molecules (N_2, CH_4, and H_2). UVIS will make a systematic survey of all the hydrocarbon species from which sources and sinks may be deduced.

The UVIS instrument will map the global distribution of UV-absorbing aerosols in Titan's atmosphere in the spectral range 160 to 190 nm. Vertical profiles of high-altitude aerosols

TABLE I
Observations by orbit period

Apoapsis	
USYSCAN	Scans of the Saturn system
USTARE	Long integrations of Saturn, Titan
UMAP	Inner magnetosphere maps
UFPSCAN	Whole sky scans during downlink
Titan	
UHIGHSN	High signal-to-noise spectroscopy of atmospheric constituents
UMAP	Maps of poles, equator, terminator, darkside, etc.
ULIMDRFT	Bright and dark limb drifts
UHDAC	Measure D/H ratio
UCSTAR	Atmospheric occultations by cool stars
UHSTAR	Atmospheric occultations by hot stars
USUN	Solar occultation
Periapse	
UHIGHSN	Spectra of rings, atmospheric features, limb, phase coverage
UMAP	Saturn N-S hemispheres, poles, etc.
URSTAR	Ring star occultation
UCSTAR	Atmospheric occultations by cool stars
UHSTAR	Atmospheric occultations by hot stars
UHDAC	Measure D/H ratio
ULIMDRFT	Limb drifts
USUN	Solar occultation
Icy Satellite	
UHIGHSN	Surface spectra
UMAP	Latitude-longitude maps
ULIMDRFT	Satellite limb drifts
UISTAR	Star occultation
USUN	Solar occultation

were seen in Titan's atmosphere by the Voyager UVS while observing a solar occultation. This type of measurement, as well as stellar occultations, will allow detailed vertical profiling of Titan's high-altitude aerosols at a variety of latitudes.

(3) *Atmospheric circulation and physics*. Atmospheric transport processes may be inferred from the spatial distribution of chemical species. UVIS will search for polar vortices via the observed gradients of chemical species. The exact variation of species abundances between the tropopause and the mesosphere depends sensitively on the nature of the vertical transport (advection and diffusion), so a precise determination of the vertical distribution of the photochemically produced species will greatly constrain models. UVIS mapping of the distribution

of hydrocarbons will reveal the dynamics of the curious seasonal behavior of Titan's atmosphere—the asymmetry between the northern and the southern hemisphere at the time of the Voyager encounter, and the polar hood.

(4) *Upper atmosphere and relation to magnetosphere*. Spectral images of UV thermospheric emission of the major nitrogen and hydrogen atmospheric species on Titan on Saturn will allow partitioning of excitation processes, determination of energy deposition (heating) rates, and ionospheric structure. The peak in emission brightness at the exobase may or may not be due to interaction with the magnetosphere, and the high spectral resolution of the UVIS EUV channel will help to answer this question: the spectral resolution of UVIS can provide a definitive separation of H_2C_4 bands and N^+ emissions, giving direct diagnostic information on excitation processes.

1.2.2. *Saturn*

(1) *Atmospheric and cloud properties and composition*. UVIS will map the global distribution of UV-absorbing aerosols in Saturn's atmosphere in the spectral range 160 to 190 nm. UVIS will determine the altitude-latitude distribution of the chemical species H, H_2, CH_4, C_2H_6, C_2H_4, and C_2H_2.

(2) *Synoptic features and processes; winds and eddies*. UVIS mapping of the hydrocarbon species will provide a basis for constructing two-dimensional models of the photochemistry, radiation and dynamics of Saturn's atmosphere. Upwelling brings the parent molecule CH_4 from the troposphere into the upper atmosphere, where it undergoes photolytic decomposition. The products will descend into the lower stratosphere, and may be partially converted into photochemical aerosols. The distribution of aerosols will be affected by the meridional circulation, which in turn is caused by radiative heating due to the hydrocarbons and the aerosols.

(3) *Ionospheric diurnal variations and magnetic control*. The aurorae on Saturn show two distinctly different morphological characteristics. Most of the Voyager observations show a high-altitude emission from 80° latitude in the north and south polar regions with an H_2-band spectrum that is remarkably similar to the emission for the sunlit equatorial region. The spectra appear to contain additional features that are compatible with transitions in N^+. Much brighter spectra from deep in the thermosphere are also observed, showing the same periodicity in apparition as the planetary rotation period. These spectra show the effects of CH_4 absorption, strong self absorption and a very weak H Lyman-α line, characteristic of excitation of H_2 with a very low [H]/[H_2] mixing ratio. This behavior and the connection to the magnetosphere are not clear, and the better resolution of the Cassini UVIS (as compared to Voyager's UVS) will yield more insight into the primary processes.

(4) *Physical and compositional properties and evolution*. In bulk composition, Saturn is a typical Jovian planet with reducing chemistry. The dominant chemistry in the upper atmosphere is the hydrocarbon chemistry initiated by the photolysis

of CH_4 and leading to the production of C_2H_6, C_2H_4, and C_2H_2. UVIS will make a systematic survey of these major carbon species as well as H atoms. Limb observations and solar stellar occultations will yield vertical profiles. Sources, sinks, and atmospheric transport processes may also be inferred from the spatial distribution of these chemical species.

(5) *Lightning*. Optical searches will be made for lightning in the FUV, in concert with other remote-sensing instruments.

1.2.3. *Rings*

(1) *Configuration and processes*. UVIS will provide high spatial resolution, low-noise stellar occultations, spectroscopy, photometry, and limited imaging of the rings. Several high-resolution (10 to 40 m), low-noise occultation opportunities at multiple azimuths will be available during each Cassini orbit. Measurement of these occultations will reveal ring structures with spatial variability on the scale of the larger abundant ring particles. The true sharpness, shape, and azimuthal variability of the many sharp edges in Saturn's rings will be measured with a spatial resolution of approximately 20 m. Ring thickness will be measured directly from oblique occultations of sharp edges. Closely spaced occultations will show the time development of spiral waves, wakes, and edge waves.

(2) *Composition and particle size*. With UVIS operating as a spectrograph, scans and drifts will yield the areal variation of UV brightness across the rings, showing compositional or age differences and the presence of submicron particles as postulated to form the spokes. Variations in reflectance can be interpreted in terms of the individual particle properties like albedo and phase function, because the radial profile of extinction optical depth will be known from the occultations.

(3) *Interrelation with satellites*. The presence or absence of phase shifts in edge waves will be determined from closely spaced occultations. The effects of imbedded or nearby moonlets will be detected in the F ring and in the similar rings in the gaps and the C ring region.

(4) *Dust and meteoroid distribution*. Photometric and spectroscopic studies will identify the emissions of H and O near the rings. Since the rings are mostly water ice, this provides a constraint on ring erosion rates. Submicron dust will be visible in the UV: the spectral variation of reflected sunlight will establish the number and size of dust particles near the rings.

(5) *Interactions with Saturn magnetosphere, ionosphere, and atmosphere*. Saturn receives oxygen and nitrogen species from the magnetosphere and the rings; thus, CO and HCN are predicted to exist in the upper atmosphere.

1.2.4. *Icy Satellites*

(1) *Characteristics and geological histories*. Regional units may be differentiated by their UV reflectance. Darkening in the UV may be an indicator of surface age and exposure to radiation.

(2) *Mechanisms of modification*. UVIS limb drifts and stellar occultations will be used to detect the existence of tenuous, possibly transient atmosphere, whose source may be surface activity, sputtering, or seasonal sublimation.
(3) *Composition and distribution of surface materials*, *especially dark, organic-rich condensates*. UV reflectivity will be used to identify and/or constrain possible composition of surface materials. The overall phase function of surface materials, including the UV, is important in determining the fine structure and degree of compaction of surface materials.
(4) *Interactions with magnetosphere and rings*. UVIS will map H Lyman-α throughout the Saturnian system as well as emissions from neutrals and ions, by acquiring data during downlink rolls. A full sky map will identify the sources of particles being detected *in situ* by the MAPS (magnetosphere and plasma science) instruments. Heavy atomic species are known to be present in the magnetosphere. It has been argued that the heavy ions are mainly O^+, derived from sputtering of the icy satellite surfaces and subsequent H_2O chemistry.

1.2.5. *Magnetosphere*

The mass content of the Saturn magnetosphere is determined almost entirely by sources internal to the Saturn system. The magnetosphere reflects the dynamic processes in the atmospheres and surfaces of the planet and satellites, which in turn are influenced by interaction with the magnetosphere in a partially closed system. Measurement of the content of neutrals and ions in the magnetosphere can provide critical information on basic atmospheric evolutionary processes as well as definition of magnetospheric structure. An understanding of this complex interactive system will clearly require knowledge of the composition, distribution, and dynamics of the magnetospheric particles. Because of the sensitivity to very weak emissions and ability to observe the entire magnetosphere remotely, UVIS will make a unique contribution to this understanding.

(1) *Configuration of magnetic field and relation to Saturn kilometric radiation*. UVIS will map H Lyman-α throughout the Saturnian system as well as emissions from neutrals and ions by acquiring data during downlink rolls. A full sky map will identify the sources of particles being detected *in situ* by the MAPS instruments.
(2) *Charged particle currents, compositions, sources and sinks*. Atomic H, which is present in significant quantities in Saturn's magnetosphere, has a complex three-dimensional distribution. Lyman-α mapping by UVIS will establish the relative dominance of the hydrogen sources (e.g., Saturn exosphere, Titan, satellites, rings). UVIS will be able to detect emissions from N^+, N^{++}, O^+, and O^{++}.
(3) Wave-particle interactions and dynamics. None identified.
(4) *Interactions of Titan's atmosphere and exosphere with surrounding plasmas*. Spectral images of UV thermospheric emission of the major nitrogen and hydrogen atmospheric species on Titan and Saturn will allow partitioning of

excitation processes, determination of energy deposition (heating) rates, and ionospheric structure. The peak in emission brightness at the exobase may or may not be due to interaction with the magnetosphere, and the high spectral resolution of the UVIS EUV channel will help to answer this question: the spectral resolution of UVIS can provide a definitive separation of H_2C_4 bands and N^+ emissions, giving direct diagnostic information on excitation processes.

1.3. Summary

In summary, the UVIS investigation has a broad range of scientific objectives encompassing the origin and evolution of the planets and their atmospheres, clouds and aerosols, magnetospheres, thermospheres and exospheres, satellite surfaces and their tenuous atmospheres, and ring structure, composition, and histories. These various objectives overlap—Titan, the rings, and satellites are sources of magnetospheric neutrals; lost atmospheric gases may be retained in the Saturn system; and magnetospheric constituents bombard and modify the rings and satellites. Furthermore, UVIS provides just one segment of the broad range of new scientific information to come from the orbiter's complement of *in situ* and remote measurements and from the Titan measurements by the Huygens probe. A major result of the UVIS investigation will be to contribute to the advance of knowledge of the Saturn system from the Cassini-Huygens mission through collaborative studies.

This paper gives a brief description of the UVIS experiment, its science objectives, and its planned observations.

2. Instrument Description

In this section, we describe the optical configuration and performance of the UVIS that enables the scientific investigation (McClintock *et al*., 1992, 1993). The UVIS design represents a balance between the science objectives and the constraints of mass, power, volume, and operability for a spacecraft instrument. Figures 1 and 2 and Table II summarize the optical and mechanical characteristics of the instrument. UVIS consists of two moderate-resolution telescope-spectrographs covering the wavelength ranges 56 to 118 nm (extreme ultraviolet, or EUV) and 110 to 190 nm (far ultraviolet, or FUV), a sensitive High Speed Photometer (HSP), and a Hydrogen Deuterium Absorption Cell (HDAC). The four separate channels are aligned for simultaneous observation.

To meet the breadth of science objectives, UVIS uses a variety of observation techniques. These include producing maps and images by moving the slit to a sequence of locations through rastering, slewing, and drifting the spacecraft optical axis. Limb drifts provide high spatial resolution at the target's limb. Occultations of the sun are observed with the EUV channel; the HSP can observe stellar occultations in concert with the EUV and FUV channel spectrographs.

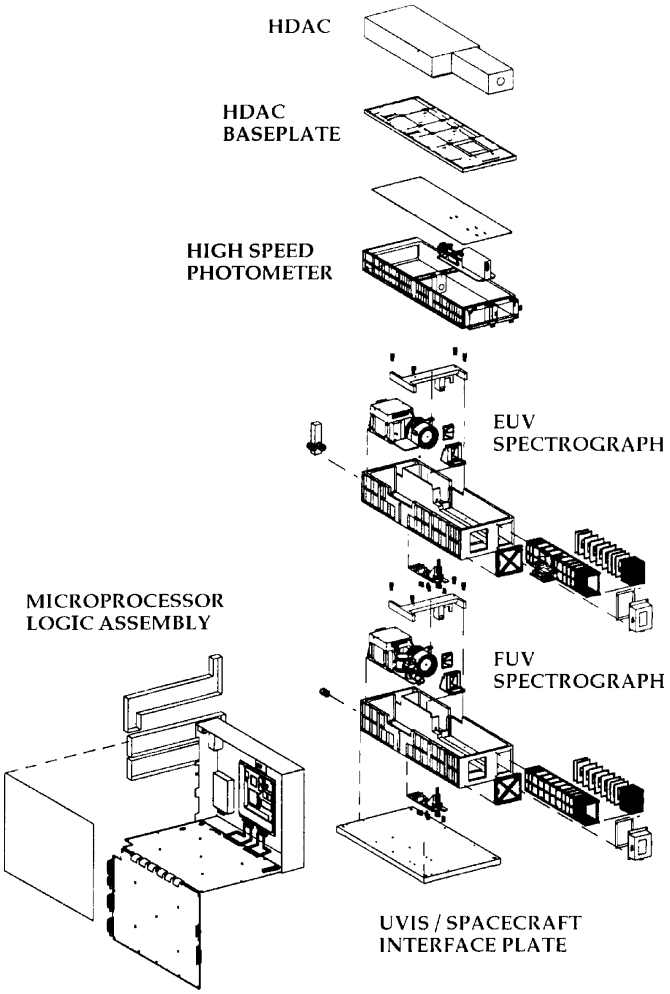

Figure 1. UVIS instrument: two spectrographs, a high speed photometer, and a hydrogen absorption cell.

UVIS will encounter a wide range of signal strengths. Saturn system atmospheric and magnetospheric emissions at wavelengths shorter than 200 nm are very faint, with radiances of the order of 0.1 to 10 Rayleighs in individual emission lines. In contrast, sunlight scattered from the disk of Saturn and its icy satellites produces radiance in the range of 1 to 10 kR/nm.

2.1. Spectrographic Channels

The basic instrument design adapts proven design concepts using a grating spectrometer followed by a multi-element detector. We chose to use imaging,

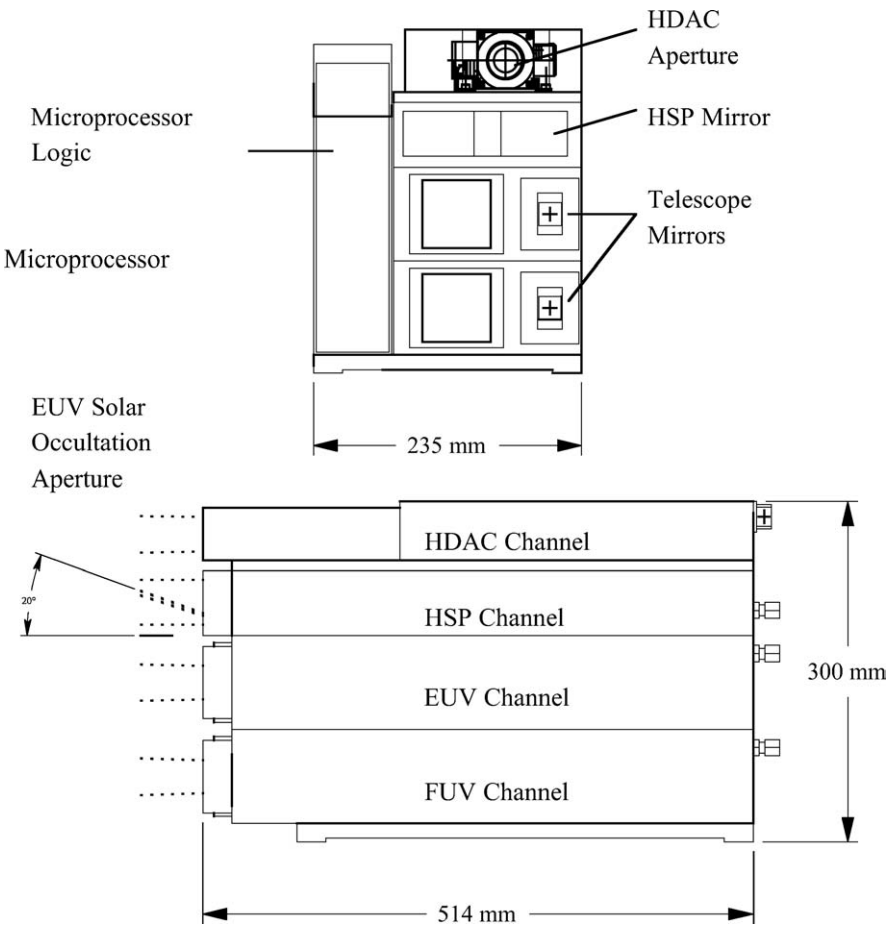

Figure 2. UVIS optical-mechanical configuration. The four channels share the same boresight. In solar occultation mode, a pick-off mirror allows sunlight to enter the EUV channel without striking the primary.

pulse-counting microchannel plate detectors because of more than a decade of experience using this kind of detector equipped with a CODACON readout anode.

2.1.1. *CODACON Detector*

The CODACON (Coded Anode Array Converter) acts as a photon locator. For $2^M \times 2^N$ pixels on the anode array, the output electronics generate a logic compatible $M + N$ bit address for each detected photon. The located photon counts are accumulated in an external memory to build a picture that is periodically read out for transfer to the spacecraft memory and eventually, the ground. The spectrograph detectors have a count rate limit of 10^5/s, set by the speed of the detection electronics. Details of the CODACON operation are described by McClintock *et al*. (1992) and Lawrence and McClintock (1996).

TABLE II
UVIS spectrographic channels and HSP

	FUV (1115–1912 Å)	EUV (563–1182 Å)	HSP	
Telescope				
Focal length size (mm)	100	100	200	
Entrance pupil size (mm)	20 × 20	20 × 20	135 × 30	
Reflecting surface	Al + MgF_2	Boron carbide	Al + MgF_2	
Toroidal gratings				
Size (mm)	60 × 60	60 × 60		
Grating radii (mm)	300, 296.1	300, 296.8		
Grating surface	A1 + MgF_2	Boron carbide	1068	1371
Grooves/mm	1068	1371		
Input angle α (degrees)	9.22	8.03		
Out angles β (degrees)	±2.9	−4.08 + 1.72		
3-Position slits				
Slit widths (microns)	75, 150, 800	100, 200, 800	6 × 6	
$\Delta\lambda$(Å) (Extended source)	2.75, 4.8, 24.9	2.75, 4.8, 19.4		
Field of view (mrad)	(.75, 1.5, 8) × 60	(1, 2, 8) × 59		
Detectors				
Photocathode	CsI	KBr	CsI	
% Maximum QE	8	25	10	
Detector window	MgF_2	none	MgF_2	
Detector size (mm)	25.6 × 6.4	25.6 × 6.4	11.0 dia	
Pixel format ($\lambda \times \theta$)	1024 × 64	1024 × 64		
Pixel size (μ)	25 × 100	25 × 100		
Pulse resolution	10 μsec	10 μsec	50 n sec	
UVIS characteristics				
Mass	15.6 kg			
Volume (L × W × H)	50.8 cm × 23.5 cm × 30.5 cm			
Power	8 W (average), 12 W (peak)			

The two-dimensional format for the CODACON detectors allows simultaneous spectral and one-dimensional spatial coverage. The detector format is 1024 × 64 (spectral by spatial) with a pixel size of 25 × 100 mm. Two separate detectors span the instrument's wavelength range, as follows. A windowless detector is required for the EUV wavelength range 56 to 118 nm. We chose KBr as the photocathode material for this detector because of its ability to withstand a moderate amount of exposure to atmospheric water vapor. CsI was also considered as the EUV photocathode, but it requires a door with a hermetic seal to protect it before launch. CsI is the photocathode material for the FUV wavelength range, 110 to 190 nm. This detector is enclosed in a separate vacuum housing with a MgF_2 window.

Although other materials such as CsTe are more efficient photocathodes than CsI for wavelengths longer than 130 nm, we use CsI for the FUV because it is much less sensitive to longer wavelength scattered light within the spectrograph. This scattered light usually dominates and can often obliterate weak planetary FUV emissions when a CsTe or a more red-sensitive photocathode is used.

2.1.2. *Optical Design*

The optical requirements for EUV channel spectrometers are unique because the low reflectivity of optical materials at these wavelengths requires that the number of optical elements in the system be as small as possible. Our design is a single-mirror telescope followed by an entrance slit and a concave grating used in a Rowland circle mount.

We found that the EUV channel configuration also provides satisfactory spatial and spectral resolution in the FUV channel. The two channels are identical except for the optical coatings, diffraction grating rulings, and detector photocathodes. To achieve the desired spectral resolution, the optics must provide image quality in the spectrograph dispersion direction that is comparable to the CODACON spatial resolution limit of 2 pixels (0.05 mm). Toroidal gratings used with the angle of diffraction equal to zero in the center of the detector have the best imaging properties because, for a given angle of incidence, they produce stigmatic images at two wavelengths in the focal plane.

The FUV channel is shown in Figure 3. This design represents the best compromise for spectral resolution, image quality, and instrument size. The EUV channel is identical to the FUV except that the detector window and ion pump are not present. Each telescope consists of an off-axis section of a parabolic mirror with a 100 mm focal length. A 20 × 20 mm aperture, which is 133 mm in front of the telescope mirror, acts as a Lyot stop conjugate to the grating. We have equipped the telescope

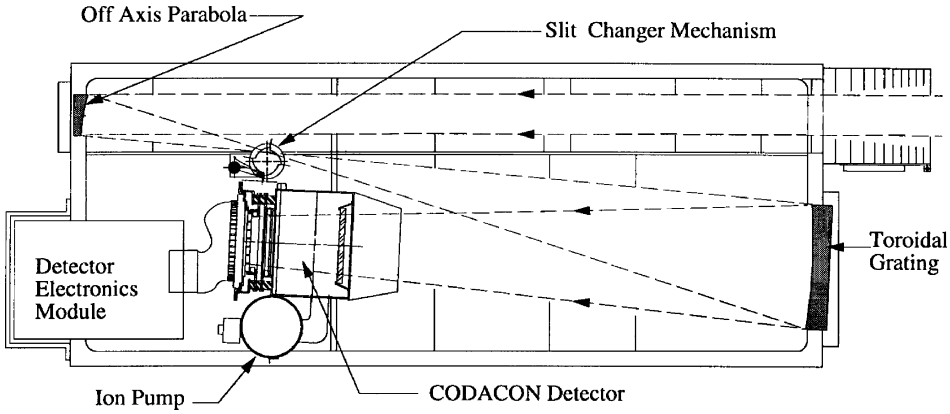

Figure 3. FUV optical configuration optimizes the trade-off between imaging and spectral resolution in the available volume.

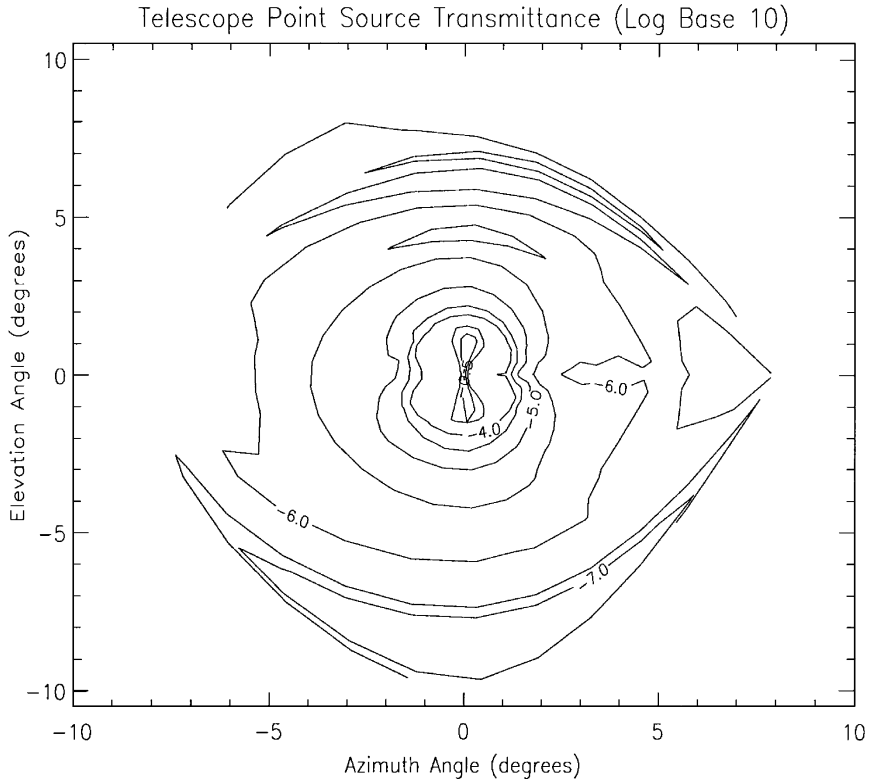

Figure 4. Contour plots of the logarithm of the telescope point source transmittance of the FUV and EUV channels.

with a sunshade and baffle system to minimize scattered light background during limb scan measurements. The point source rejection ratio, which was measured using a laboratory collimator to simulate a star, is 10^6 for sources located 1° or more away from the field of view (Figure 4).

Each spectrograph consists of a set of three interchangeable entrance slits (0.075 to 0.8 mm wide $\times$ 6.4 mm tall, see Table II) and a toroidal grating with a 300 mm horizontal radius of curvature used in a Rowland circle mount. The spectrum is thus formed on a cylinder of radius 300 mm. The detector lies on a chord of the Rowland circle to minimize average defocus over its planar 25.6 $\times$ 6.4 mm sensitive area. The grating ruling spacing is set to meet the spectral coverage requirement for each channel.

Mechanical constraints require the spectrograph housings to have the angle $\alpha - \beta$=9.2° identical for both channels (α and β are the angles of incidence and diffraction, respectively). This configuration results in $\beta = 0^\circ$ at the center of the detector for the FUV channel. The detector then subtends angles $\Delta\beta = \pm 2.45^\circ$ along the Rowland circle. The grating radii yield the stigmatic wavelengths at $\beta_s = \pm 1.23^\circ$, with the detector plane also intersecting the Rowland circle at these

wavelengths. This configuration thus yields the best average imaging over the entire detector.

2.1.3. *Spectrometer Sensitivity*

The following equations relate the signal and noise output of the UVIS spectrometer channels to their design parameters. For viewing extended sources,

$$S(\lambda) = I(\lambda) \ * \ A_{\mathrm{T}}(\lambda)/F_T^2 \ * \ A_{\mathrm{pix}} \ * \ \tau(\lambda) \ * \ QE(\lambda)T \tag{1}$$

$$N^2(\lambda) = S(\lambda) + BT \tag{2}$$

where S is the signal in counts per pixel, λ the wavelength, I the source radiance in kR (10^9 emitted photons per square centimeter per 4π steradian per second), $A_{\mathrm{T}}/F_{\mathrm{T}}^2$ the square of the optical system focal ratio, A_{pix} the area of a single detector pixel in square centimeters, τ the optical system transmission, QE the detector quantum efficiency; T the observation time in seconds; N the noise in counts per pixel, and B the detector background or 'dark count' in counts per pixel per second.

Figure 5 shows the system sensitivity of UVIS for each channel and for the high-resolution and low-resolution slit widths (each labeled by its width in μm) and spectral resolution in nm. Curves for the occultation slits (not shown) are a factor of 10.7 higher than the curves for a 75 μm slit. In limb scan mode, we orient the entrance slit parallel to the planet limb and slew the spacecraft to obtain vertical profiles, summing all 64 spatial pixels into a 1024 × 1 spectrum. Mapping mode uses the full 2-dimensional capability of the detector, and we generate a spectral-by-spatial map of 1024 × 64 pixels.

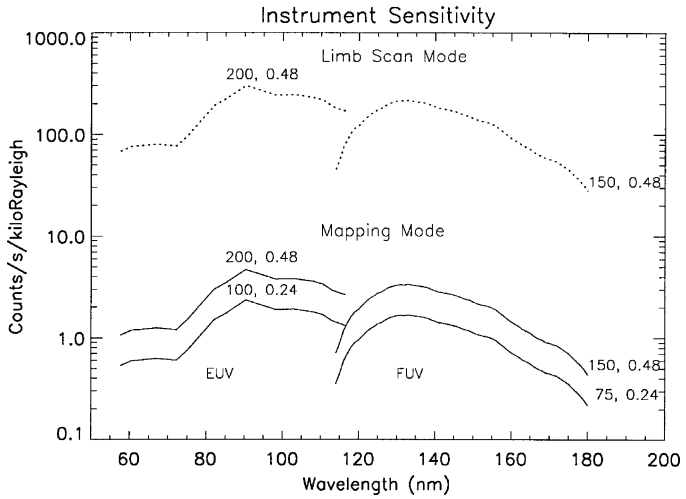

Figure 5. UVIS sensitivity in counts/second/kiloRayleigh. Each curve is labeled by the slit width (μm) and the resolution (nm). Higher sensitivity is available in limb scan mode from adding all the 64 picture elements along the slit.

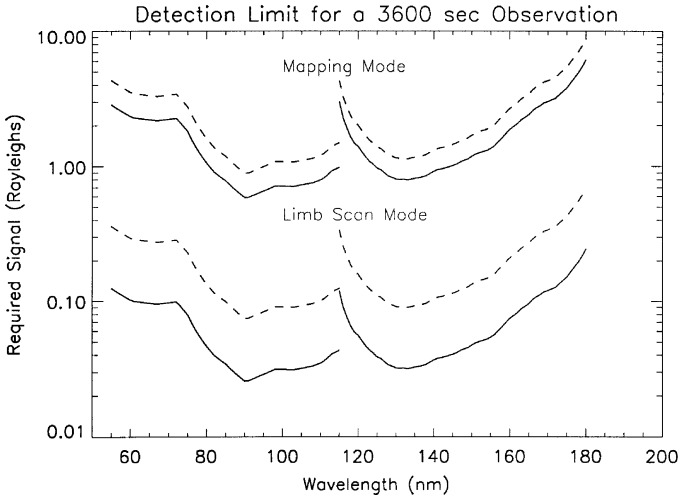

Figure 6. UVIS sensitivity limits for an integration period of one hour. Solid lines indicate low resolution and high resolution slits. Dashed lines indicate summing of all spatial information along slit.

In Figure 6, we plot the detection limit (i.e., the signal required to produce a signal-to-noise ratio of 3.0) for a 3600 s observation in limb scan and mapping modes. Solid lines are for typical observed CODACON backgrounds of 2 counts per detector (65,536 pixels) per second. The dashed lines in Figure 6 show detection limits for the total expected background, including the three Radioisotope Thermoelectric Generators (RTGs) that provide the spacecraft with electrical power. We estimate that the gamma rays emitted by the RTGs will increase the background by an additional 20 counts per detector per second. Observations during instrument check-out in 1999 gave a preliminary estimate of 35 counts.

2.1.4. *Example Spectroscopic Observations*

An example of mapping is as follows. Titan's disk has an angular diameter of 2.6° (45 mrad) at 5.2 h before closest approach (at a distance of about 1.2×10^5 km), and a single detector pixel subtends 2.5° of latitude at the subspacecraft point. The satellite just fills the length of the spectrograph entrance slit at T-3.7 h. Thus T-5.2 h to T-3.7 h is an ideal time to make maps to provide data for photochemical models and aerosol studies (see Sections 3 and 4 below).

Limb scans and atmospheric occultation measurements provide higher spatial resolution nearer to closest approach. We have good off-axis rejection of the bright disk for weak emissions if it is 5° from the optical axis. For thermosphere measurements at an altitude of 1000 km, this requires that the range must be less than 11×10^3 km. This occurs at about T-0.5 h when the high resolution, 75- μm-wide entrance slit subtends about 9 km at the limb and the spacecraft drifts about 1 scale height (50 km) every 8 s. Occultation measurements of the atmosphere can be made

at larger ranges, especially on Titan's night side, when there is minimal scattered light from the sunlit disk.

2.2. Stellar and Solar Occultation Modes

The UVIS spectroscopic channels will view stars that are occulted by the atmospheres of Saturn and Titan and by Saturn's rings. Because spacecraft pointing accuracy is estimated at ± 2 mrad, we have set each telescope field of view to be 8 mrad wide (using the occultation slit: 'Occ') for stellar occultation experiments. The field of view is selected by a three-position slit mechanism in each channel (Figure 2). Two other slit positions are provided: one that is 0.75 mrad wide (FUV) or 1.0 mrad wide (EUV) to give the highest spectral resolution requirements for extended sources ('Hi-Res'), and one that is 1.5 mrad (FUV) or 2.0 mrad (EUV) wide to provide a larger signal at less resolution ('Lo-Res').

We also added a solar occultation capability to the EUV channel; more distant stars are generally not useful at wavelengths shorter than 91.2 nm because interstellar atomic hydrogen blocks their radiation. In this observing mode (see Figure 2), light enters the EUV channel through a small aperture located 20° away from the normal viewing direction, and it is directed toward the telescope mirror by a small grazing incidence mirror. A two-position mechanism is used to block the light path when the solar viewing mode is not used.

2.3. High Speed Photometer

UVIS contains a High Speed Photometer (HSP) with an integration time of 2.0 ms to observe stars occulted by the rings of Saturn. Figure 7 shows the HSP configuration, which consists of a telescope mirror that is approximately 10 times as large as those used in the spectroscopic channels, followed by an aperture to

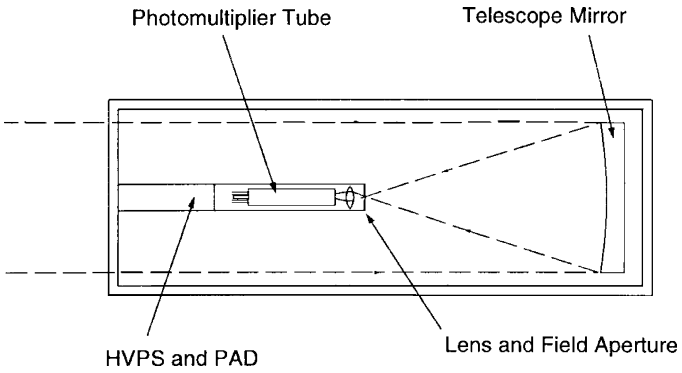

Figure 7. High Speed Photometer (HSP) layout showing High Voltage Power Supply (HVPS) and Pulse Amplifier/Discriminator (PAD).

limit the field of view to 6 mrad, a MgF_2 lens, and a Hamamatsu model R1081 photomultiplier tube with a CsI photocathode used in pulse-counting mode. The lens images the telescope mirror onto the photocathode of the photomultiplier. Without this lens, small changes in spacecraft pointing would cause the image of the star to move around on the nonuniform detector photocathode, resulting in unwanted signal variations. Figure 7 also shows the detector electronics location, which includes a High-Voltage Power Supply (HVPS) and a Pulse Amplifier Discriminator (PAD).

The spectral response of the HSP is limited at short wavelengths to about 115 nm by the MgF_2 detector window and at long wavelengths to about 190 nm by the work function of the CsI photocathode. We chose CsI for its low sensitivity to solar light, because the spacecraft orbit geometry requires that many of the occultation observations be made while looking through the sunlit rings. The photometer field of view must be at least 6 mrad to account for pointing errors of ± 2 mrad. If we used a photomultiplier with either a CsTe or a Bi-alkali photocathode with this large a field of view, sunlight reflected from the rings would produce a background at least 100 times larger than the signal from the brightest stars. Figure 8 is a contour plot of the off-axis response of the HSP. The off-axis response is roughly symmetric around the HSP boresight and drops off to 10^{-5} at 10° off axis. Using a CsI photocathode, we are limited to stars with spectral class O and B (effective temperatures in the range 10,000–40,000 K), but the background from reflected sunlight is equal to the signal from a B5 star with a visual magnitude M_{v} of 4.5. During the Saturn orbital mission, we expect over 350 stellar occultation opportunities for the rings with stars that are at least 10 times brighter than M_{v} of 4.5.

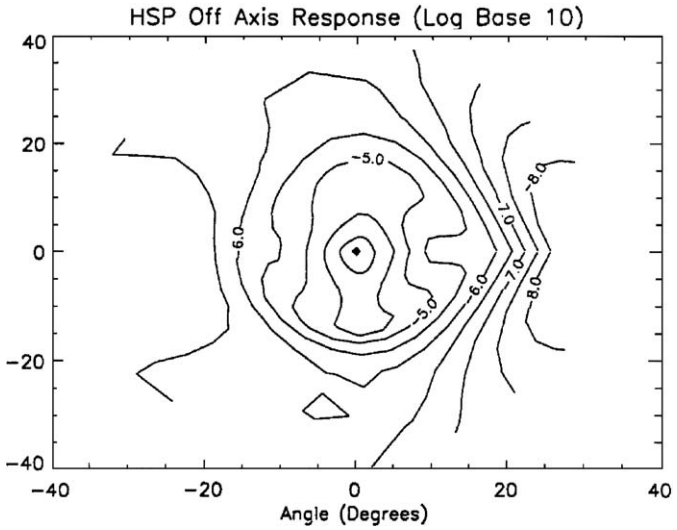

Figure 8. HSP off-axis response (contours: $\log_{10}$ of sensitivity relative to maximum signal).

2.4. HDAC Description

The first use of a hydrogen absorption cell for spaceborne remote sensing was by Morton and Purcell (1961). They used the cell as a broadband blocking filter to prove that hydrogen Lyman-α emission was present in the night sky of the Earth. Winter and Chubb (1967) used a hydrogen cell to observe the night-sky hydrogen Lyman-α line shape. In the 1970s, Bertaux flew hydrogen cells to study the line shape of hydrogen Lyman-α in planetary coronae and the local interstellar medium (LISM). These experiments included OGO-5 at Earth (Bertaux, 1978), the Soviet Venera missions at Venus (Bertaux *et al.*, 1978), the Soviet Mars missions (Babichenko *et al.*, 1977), and the Soviet Earth orbiters Prognoz 5 and 6 (Bertaux, 1977).

The only successful use of a hydrogen deuterium absorption cell to measure the deuterium-hydrogen ratio (D/H) in the Earth's atmosphere is by Bertaux *et al.* (1984) aboard Spacelab-1. Unsuccessful attempts to measure atomic D/H include Mars (Babichenko *et al.*, 1977) and Venus (Bertaux *et al.*, 1978). The cells mentioned above were made of glass. The Japanese Nozomi mission to Mars has hydrogen deuterium absorption cells similar to the Bertaux cells (Kawahara *et al.*, 1993). For information on this experiment, also see Kawahara (1994). The forerunners of the HDAC (stainless steel hydrogen cells) were developed by Hans Lauche and Wilhelm Barke of the Max-Planck-Institut für Aeronomie (MPAe) in Katlenburg-Lindau, Germany, as part of the Interzodiac program. The Teflon coating of the HDAC cells allows lighter weight and lower power, since recombination times are longer.

The Cassini HDAC channel (Figures 9 and 10), which was built at the MPAe, consists of a Channel Electron Multiplier (CEM) photodetector equipped with 3 absorption cell filters: a hydrogen cell, a deuterium cell, and an oxygen cell. The cells are separated by MgF_2 windows. The oxygen cell was designed to be a static

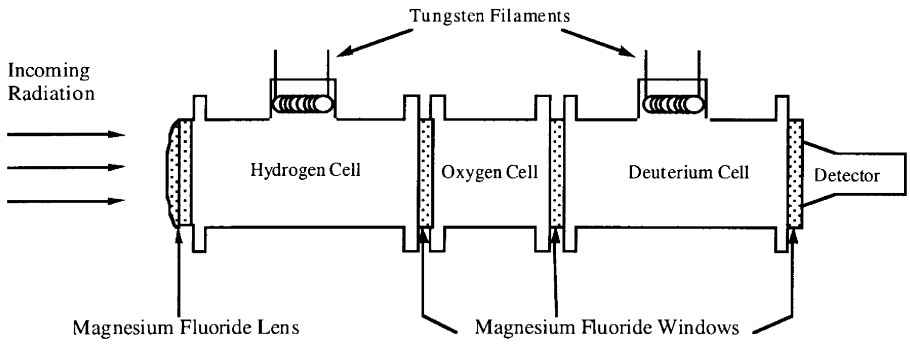

Figure 9. Conceptual diagram of the Cassini Hydrogen Deuterium Absorption Cell (HDAC). The tungsten filaments dissociate molecular hydrogen and deuterium inside the cells. The dissociated atoms resonantly absorb hydrogen and deuterium Lyman-α. Cycling the filament currents in both the hydrogen and deuterium cells gives a direct measurement of the hydrogen and deuterium Lyman-α intensities.

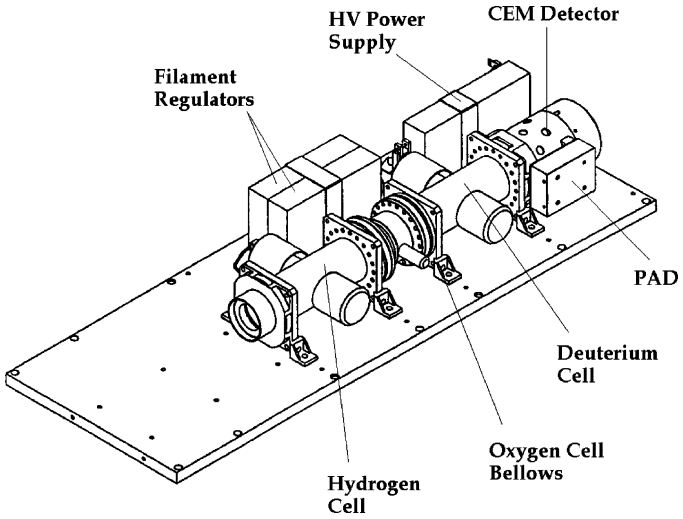

Figure 10. The Cassini HDAC without baffle and cover.

broadband filter from 1150 to 1800 Å but was unfortunately vented prior to flight due to contamination caused by water vapor accumulating in the O_2 cell. The hydrogen and deuterium cells function as adjustable absorption filters, as described below.

In each cell, a hot tungsten filament dissociates the H_2 and D_2 molecules into atoms, producing an atomic density dependent on the filament temperature. These atoms resonantly absorb the hydrogen and deuterium Lyman-α lines (located at 1215.67 Å and 1215.34 Å) passing through the cells. Cycling the filaments on and off and comparing the differences in signal gives a direct measurement of the relative hydrogen and deuterium signals. For an analysis and calibration of the Cassini HDAC absorption cell, see Maki (1996).

The cells are mounted on an anodized aluminum baseplate along with a baffle attached to the front of the hydrogen cell. At the entrance to the HDAC, a single MgF_2 lens focuses the incoming light. The lens and windows are laser-welded into the ends of the cell bodies, and the cells are connected by flanges. The cells are filled to approximately 1.2 mbar pressure. Each cell has two filaments controlled by separate filament current regulators for each cell. The two regulators are essentially low-voltage power supplies that set and regulate the power into the filaments. Only one filament at a time per cell is used during flight. A Pulse Amplifier Discriminator detects photoelectrons from the CEM and sends pulses to the UVIS instrument logic.

2.5. Measuring D/H with the HDAC

The optical depth τ of an HDAC cell at line center is $\tau = \sigma n_{\mathrm{H}} L$, where σ is the photoabsorption cross section, n_{H} is the number density of the atoms, and L is the

TABLE III

Hydrogen atom density and the corresponding number of atoms in a 300 K hydrogen absorption cell for various values of optical depth.

Optical depth	Atomic hydrogen density (atoms/cm^3)	Number of dissociated hydrogen atoms in a single HDAC absorption cell
0.5	1.7×10^{11}	7.5×10^{12}
1	3.5×10^{11}	1.5×10^{13}
5	1.7×10^{12}	7.5×10^{13}
10	3.5×10^{12}	1.5×10^{14}

Note. The number of dissociated atoms is much smaller than the total number of molecules in the cell (10^{18}). The maximum optical depth of the HDAC is less than 20 (see Section 2.4).

TABLE IV

Measured HDAC flight unit optical depths for the hydrogen and deuterium cells (Maki, 1996)

	Hydrogen cell		Deuterium cell	
Step	τ_H	τ_D	τ_H	τ_D
1	0.15	0.0	0.3	0.02
2	0.8	0.0	1.5	0.16
3	1.4	0.0	2.7	0.25
4	2.1	0.0	4.3	0.37
5	4.8	0.0	10.0	0.87
6	6.0	0.0	11.0	1.06
7	7.0	0.0	13.0	1.28

path length (8.5 cm). For the HDAC hydrogen cell at 300 K, $\sigma = 3.4 \times 10^{-13}$ cm^2. Table III shows the hydrogen atom density for selected values of optical depth. The transmission of the cell at line center is given by $T = e^{-\tau}$. See Table IV for the measured values of the flight HDAC optical depth as a function of filament step. Transmission as a function of wavelength is given by

$$T(\lambda) = e^{-\tau\phi(\lambda)}, \quad \text{where } \phi(\lambda) = e^{-\frac{x^2}{\Delta\lambda_D^2}} \tag{3}$$

where $\Delta\lambda_D$ is the Doppler width.

Because the HDAC is sensitive to electromagnetic radiation over a wide spectral range, the signal generated by the HDAC is directly proportional to the integrated intensity of the incoming radiation over this region. The total signal is expressed as

$$I = \int_{-\infty}^{\infty} S(\lambda)H(\lambda)T(\lambda)\,d\lambda \tag{4}$$

where I is the signal from the photometer, $H(\lambda)$ is the intensity of the radiation as a function of wavelength, $S(\lambda)$ is the sensitivity of the photometer, and $T(\lambda)$ is the transmission of the filter as a function of wavelength. The ratio of the modulated intensity I to the unmodulated intensity I_0 (assuming no background) is given by the reduction factor R:

$$R = \frac{I}{I_0} = \frac{\int_{-\infty}^{\infty} S(\lambda)H(\lambda)T(\lambda)\,\mathrm{d}\lambda}{\int_{-\infty}^{\infty} S(\lambda)H(\lambda)\,\mathrm{d}\lambda} \tag{5}$$

When no power is applied to the filament, the absorption cells contain only molecules, and the cells are transparent to incoming radiation at Lyman-α. When power is applied to the filament in the cell, the molecules dissociate into absorbing atoms, which block incoming radiation at Lyman-α. This process defines a negative filter; subtracting this filter profile from unity gives an effective filter, $I_0 - I$, which is:

$$I_0 - I = \int S(\lambda)H(\lambda)(1 - T(\lambda))\,\mathrm{d}\lambda \tag{6}$$

Note that in general, the background level will be unknown and will be determined by taking the differences between the modulated and unmodulated signals.

In addition to measuring the ratios of the deuterium and hydrogen Lyman-α lines, the Cassini HDAC, as a high resolution spectrometer, has the ability to measure the Lyman-α line shapes. Because instrument filter functions have different shapes for each filament level, a full cycle through the filament settings produces a set of filters that probes the line shape of the incoming radiation. Additionally, the range of spacecraft Doppler velocities scans these filter functions through the line.

2.6. HDAC Calibration

2.6.1. *Lyman-α Sensitivity*

The sensitivity $S_{\mathrm{Ly}\alpha}$ of the instrument is the count rate per input flux:

$$S_{\mathrm{Ly}\alpha} = \frac{10^6}{4\pi} \cdot QE \cdot \Omega \cdot T_{\mathrm{W}}^3 \cdot T_{\mathrm{L}} \tag{7}$$

where $S_{\mathrm{Ly}\alpha}$ is in units of counts/sec/Rayleigh, QE is the quantum efficiency of the detector in units of counts/photon, Ω is the solid angle subtended by the HDAC FOV in units of steradians, $T_{\mathrm{W}}^3 \cdot T_{\mathrm{L}}$ is the transmission of the three windows and the single lens, and A is the area of the front lens in units of cm^2. The value of $S_{\mathrm{Ly}\alpha}$ (as measured in the laboratory using a calibrated NIST windowed UV photodiode) is (30 $\pm$ 10) counts/sec/Rayleigh.

2.6.2. *Broadband Sensitivity*

The red tail of the HDAC is the sensitivity of the instrument to electromagnetic radiation redder than 1216 Å. The broadband spectral sensitivity of the HDAC is

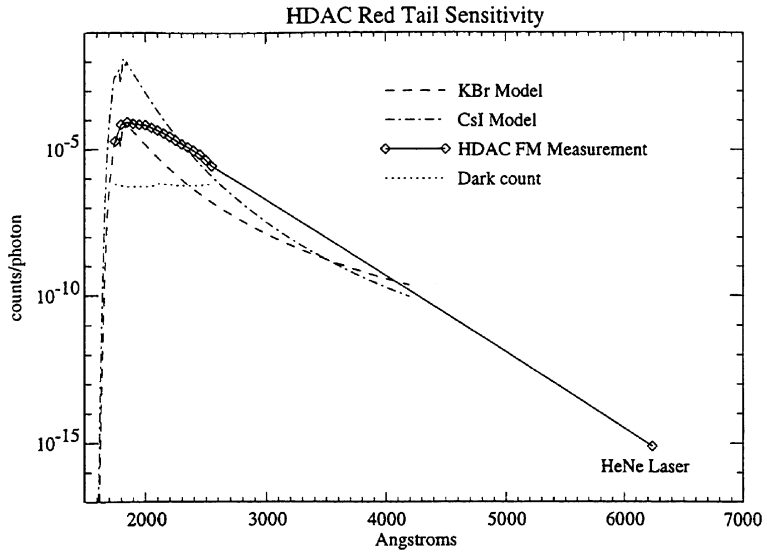

Figure 11. HDAC on-axis red tail sensitivity. Because detector red tails typically decrease with time, this value for the sensitivity is an upper limit. The dash dot and dashed lines represent the modeled sensitivity for an HDAC with a CsI and KBr detector, respectively. The detector in the HDAC Flight Model (FM) has a KBr photocathode, implying that the FM red tail curve may eventually fall on the modeled curve for KBr. The dotted line at 10^{-6} counts/photon is the dark count of the detector divided by the number of photons in the beam, the lowest sensitivity value that could be measured in this particular experiment.

bracketed on the blue side by the MgF_2 windows, which absorb radiation below 1150 Å. The value for the sensitivity of the instrument from 1750 Å to 2400 Å is important, because at this point the UV output of the sun begins to increase rapidly with wavelength. Because the signal from the reflected solar background radiation is an important component in the determination of the signal-to-noise ratio of HDAC data, a KBr (potassium bromide) detector was chosen because it possesses the combination of low detector sensitivity to solar radiation and high sensitivity to Lyman-α. When making observations of planetary atmospheres, the background signal in the red tail region is determined by a competition between the increasing solar output and the decreasing photocathode sensitivity. If the photocathode efficiency decreases fast enough relative to the solar output, the solar contribution to the background will be minimal. If however, the photocathode efficiency decreases too slowly, the background from the sun can dominate and Lyman-α observations will be difficult due to the low signal-to-background ratio. Measurements of the HDAC red tail are shown in Figure 11. The red-tail sensitivity of CEM detectors of this type has been known to increase over the timescale of sev eral years (Hans Lauche, personal communication). We are monitoring possible changes in the red tail by performing in-flight calibrations. The measurements are above the predicted KBr response, but may decay to the model curve with use.

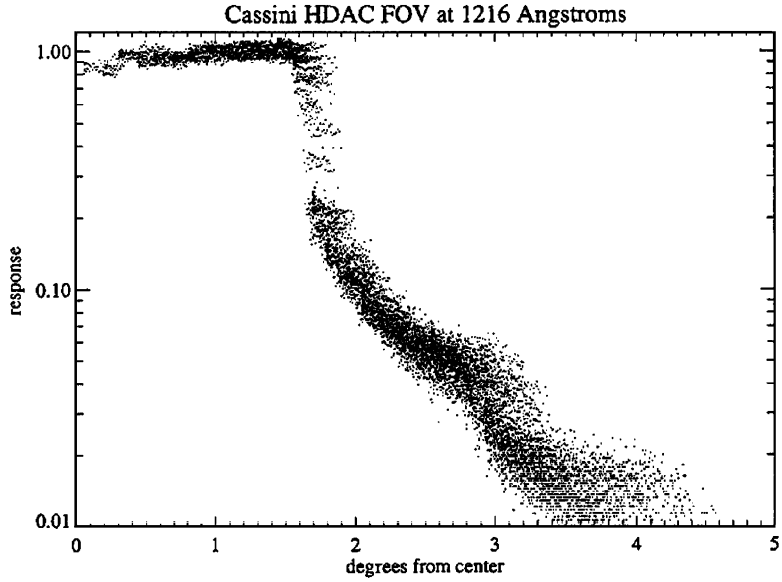

Figure 12. The HDAC off-axis radiometric response at 1216 Å.

2.6.3. *Off-Axis Response*
The HDAC off-axis response was measured at two wavelengths (1216 Å and 2537 Å) using a pan/tilt calibration fixture. See Figure 12 for a plot of the HDAC off-axis response at 1216 Å.

2.6.4. *In-flight HDAC Performance*
To date, HDAC has had several checkout and calibration activities in flight. Unfortunately, these activities were dissimilar to those we plan during the Saturn tour, and some behavior was unexplained. Thus, we are engaged in further testing and HDAC observations of the interstellar medium, Jupiter, and stellar sources to better define the HDAC performance and confirm its capability to meet the science measurement objectives for D/H at Titan.

3. Chemical Composition in the Atmospheres of Titan and Saturn

A unifying theme that relates our atmosphere to all planetary atmospheres in the solar system is to understand their origin, composition, and evolution. All planets share a common origin about 4.6 billion years ago. The subsequent divergence in the solar system may be attributed to initial conditions and subsequent evolution. A comprehensive survey of the chemical composition of all planetary atmospheres, including that of the Earth, has recently been carried out by Yung and DeMore (1999). Unfortunately, most of the evidence for atmospheric

evolution in the solar system has not been preserved. Since Saturn and Titan were derived from materials in the same region of the solar nebula, and the two atmospheres were subjected to the same solar radiation over the age of the solar system, the comparative study of the chemical composition of the atmospheres of Saturn and Titan offers a unique opportunity to explain planetary composition.

3.1. Comparison of Saturn and Titan

The atmosphere of Saturn is composed primarily of the lightest elements, hydrogen and helium, which were captured from the solar nebula during formation. The planet has a rocky core made of heavier elements. However, the mass of the gas greatly exceeds that of the core. Due to the enormous gravity of the giant planet, little mass has escaped from its atmosphere. Hence, the bulk composition is expected to provide a good measure of the initial composition of the solar nebula. Recently, significant departures (by factors of 2 to 3) from the solar values for the heavy elements C, N, P, and S have been observed for Jupiter and presumably for Saturn (Owen *et al*., 1999; Atreya *et al*., 1999; Orton *et al*., 2000). The enhancement of O is not confirmed because the Galileo probe entered an unusually dry part of the atmosphere of Jupiter (Showman and Ingersoll, 1998). An influx of icy planetesimals formed at low temperature ($T < 30$ K) might have been responsible for the enrichment of heavy elements.

Titan was formed in the Saturnian sub-nebula at the time of the formation of Saturn. Due to the lower temperatures in this region of the solar nebula, ices were common, and Titan (like Saturn) accreted material that is rich in ices. As the atmospheric constituents are photochemically processed and converted into condensible material, the ices on the surface or outgassing from the interior must maintain the supply of gas to the atmosphere. Titan possesses a thick, mildly reducing atmosphere that is different from the atmosphere of Saturn in at least two aspects. First, there is little H_2 in the atmosphere of Titan relative to the most abundant gas, N_2. The gravity is low enough that light gases like H and H_2 did not accumulate at formation. In contrast, the composition of Saturn is dominated by H_2. Second, unlike Saturn, Titan has a cold, solid surface. Organic compounds that are synthesized in the atmosphere are deposited on the surface, resulting in their permanent sequestration. This implies an irreversible chemical evolution of the atmosphere and the surface. Titan has no recycling of organic species as in Saturn. The atmosphere is being gradually destroyed by photolysis and must be resupplied by primordial ice on the surface or outgassing from the interior.

The net result of the photochemical destruction of CH_4 is its conversion to higher hydrocarbons. Ultimately the product species gain molecular weight and become heavy enough to condense, giving rise to a ubiquitous aerosol layer in the atmosphere known as Axel-Danielson dust. The Titan aerosol chemistry

is augmented by the coupled chemistry of CH_4 and N_2, resulting in the formation of nitrile compounds. The presence of an aerosol layer in the atmospheres of Saturn and Titan has profound consequences for the thermal budget of the upper atmosphere. Indeed, aerosol heating is a primary cause of the thermal inversion in the atmospheres of Saturn and Titan above the tropopause. The aerosols may also present a surface for possible heterogeneous chemical reactions.

The previous major advance in our knowledge of Saturn and Titan is from the Voyager encounters, summarized in special issues of Science (Voyager 1, 1981, Voyager 2, 1982) and the Journal of Geophysical Research (Voyager 2, 1983). The Cassini mission offers a unique opportunity to expand the base of knowledge from previous missions and Earth-based observations and to make new fundamental discoveries. One of the most important contributions of the Cassini observations is a comparison of the thermal structure and photochemistry of Titan and Saturn. There are at least three important aspects of the chemistry of Saturn and Titan: the hydrocarbon chemistry, the oxygen chemistry, and the nitrogen chemistry.

3.2. Thermal Structure

Figures 13a and b show the temperature and bulk number density of the atmospheres of Saturn and Titan as a function of altitude. Unless otherwise stated, all Saturn and Titan data in the figures are from Moses *et al.* (2000) and Yung *et al.* (1984). The temperature at the top of the Saturn atmosphere is uncertain; two values have been reported: 420 K (Smith *et al.*, 1983) and 700 to 800 K (Atreya *et al.*, 1988). The results based on Voyager (see special issues referenced above) reveal several prominent common features of the thermal structure that are so distinctive as to be the basis for dividing the atmosphere into regions. The region from the reference level to the temperature minimum is known as the troposphere, where the temperature decreases with altitude. The troposphere is characterized by vigorous convective activities. Above the tropopause is the stratosphere, where the temperature increases to a maximum around 400 km. The inversion is caused by the absorption of sunlight by aerosols and has the effect of inhibiting mass exchange between the stratosphere and other parts of the atmosphere. Above this, the temperature decreases again in the mesosphere to a second minimum near the mesopause (around 800 km). Above the mesopause, the temperature rises again in the thermosphere.

The most interesting aspects of the thermal structure of Saturn and Titan are the thermal inversions in the stratosphere and the thermosphere. The principal heat absorbers in the stratosphere are CH_4 and the Danielson-Axel aerosols. Titan has more aerosols, and its stratosphere is therefore warmer. A quantitative relation between the composition and the heat budget remains to be established from more precise measurements.

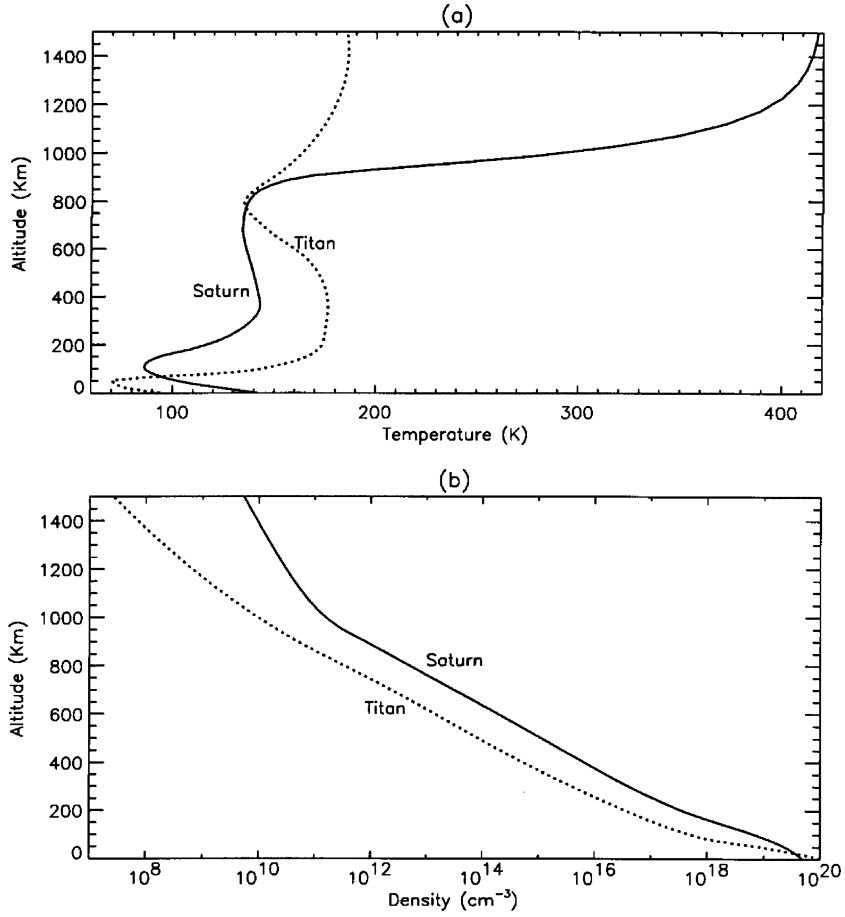

Figure 13. (a, b) Temperature profiles in the atmospheres of Saturn and Titan. Zero km refers to the 1 bar level on Saturn and 1.5 bar (the surface) for Titan. A possible higher temperature of Saturn's upper atmosphere of 700 K to 800 K (Atreya *et al.*, 1988) is not shown.

The hot thermosphere of Saturn is a puzzle (Festou and Atreya, 1982). In the terrestrial atmosphere, the high temperature can be explained by solar heating balanced by cooling due to conduction. This appears to be an adequate explanation for the thermospheric temperature on Titan, but not for Saturn, because it implies a very large eddy diffusion coefficient. An additional heating mechanism, such as that associated with the viscous damping of upward propagating waves from the troposphere, may be needed to account for the hot thermosphere of Saturn (Young *et al.*, 1997). To quantify this mechanism, we need observations of gravity waves, as manifested in the vertical structure of temperature and the vertical profiles of chemical species in the mesosphere and lower thermosphere. This can best be accomplished by UVIS solar or stellar occultations.

3.3. PHOTOCHEMISTRY

The photochemistry of hydrocarbons in the atmosphere of Jupiter has been studied in a comprehensive model that includes all the relevant chemistry up to 8 carbon atoms and vertical transport by eddy diffusion (Gladstone *et al.*, 1996). As one of the four giant planets, Saturn's photochemistry should be similar to that of Jupiter. The chemical model for Jupiter has recently been extended to Saturn by Moses *et al.* (2000). The major changes in the model include the new chemistry of oxygen species that have been detected by the Infrared Space Observatory (ISO) (Degraauw *et al.*, 1997). The photochemistry of hydrocarbon, oxygen, and nitrogen species on Titan was modeled by Yung *et al.* (1984) in a comprehensive chemical model that incorporated all the observations of the Voyager available at that time. Since then, there have been updates and extensions of that model based on subsequent Voyager analysis (Coustenis and Bezard, 1995; Coustenis *et al.*, 1989, 1991), and further analysis of data (Lara *et al.*, 1996), as well as laboratory kinetic studies (e.g., Zwier and Allen, 1996). These results will be briefly discussed in their relation to a comparative study of Saturn and Titan by Cassini.

3.3.1. *Hydrocarbon Chemistry*

Figures 14a and b show the principal hydrocarbon species in the atmosphere of Saturn. Methane is the parent molecule of all hydrocarbons in the model. Its mixing follows the bulk density of the atmosphere (see Figure 14a). Rapid destruction occurs around and above the homopause, which is at an altitude of 1110 km (Atreya, 1982). The destruction of CH_4 gives rise to the production of radical species, which eventually recombine to form C_2H_6, C_2H_4, C_2H_2 (Figure 14a) and heavier species C_3H_8, C_4H_2 and C_4H_{10} (Figure 14b). We note that the alkanes (C_2H_6, C_3H_8, C_4H_{10}), once formed, are stable; their concentrations are high in the stratosphere. But the unsaturated hydrocarbons (C_2H_2, C_2H_4, C_4H_2) are less stable. They are destroyed before they reach the lower stratosphere. All higher hydrocarbon species are rapidly removed below the tropopause by rapid transport to the interior of the planet, where they are recycled back to the thermodynamically most stable product, CH_4. Since CH_4 is originally derived from the deep atmosphere, this constitutes a closed loop; there is negligible loss of even the lightest molecules.

Figures 15a and b show the principal hydrocarbon species in the atmosphere of Titan. Comparing with Saturn, we note that the efficiency of organic synthesis is much higher in Titan, even though the total rate of CH_4 photolysis (the primary driver of photochemistry) is the same. The main reason is that Saturn's atmosphere is dominated by H_2, whereas Titan's atmosphere is dominated by N_2. This will become clear if we examine the comparison between atomic hydrogen profiles in the atmospheres of Saturn and Titan (Figure 16). The lower concentration of H atoms on Titan is due to their escape from Titan. As a result, the back reaction:

$$H + CH_3 + M \rightarrow CH_4 + M \quad (8)$$

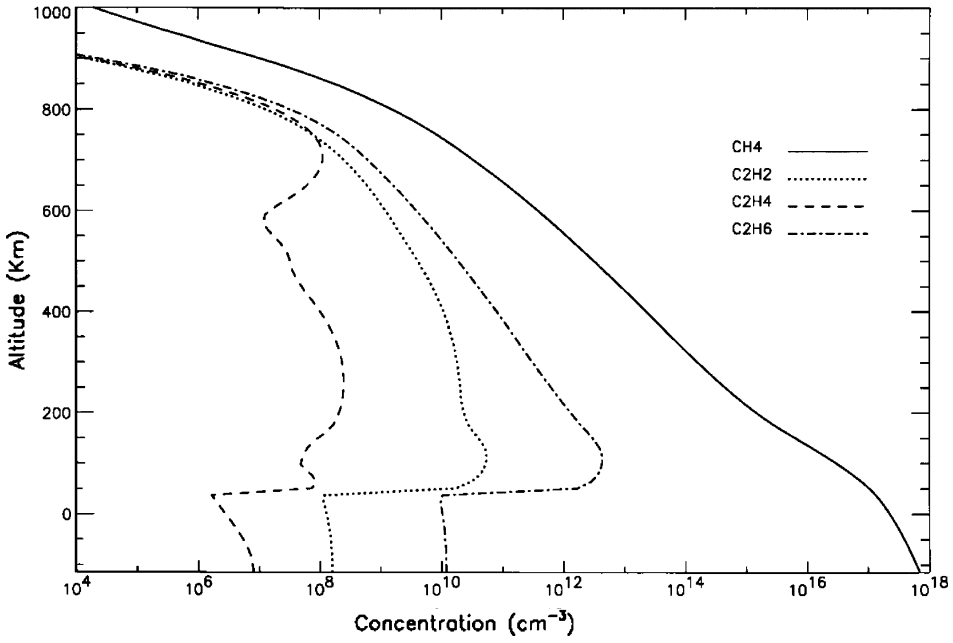

(a)

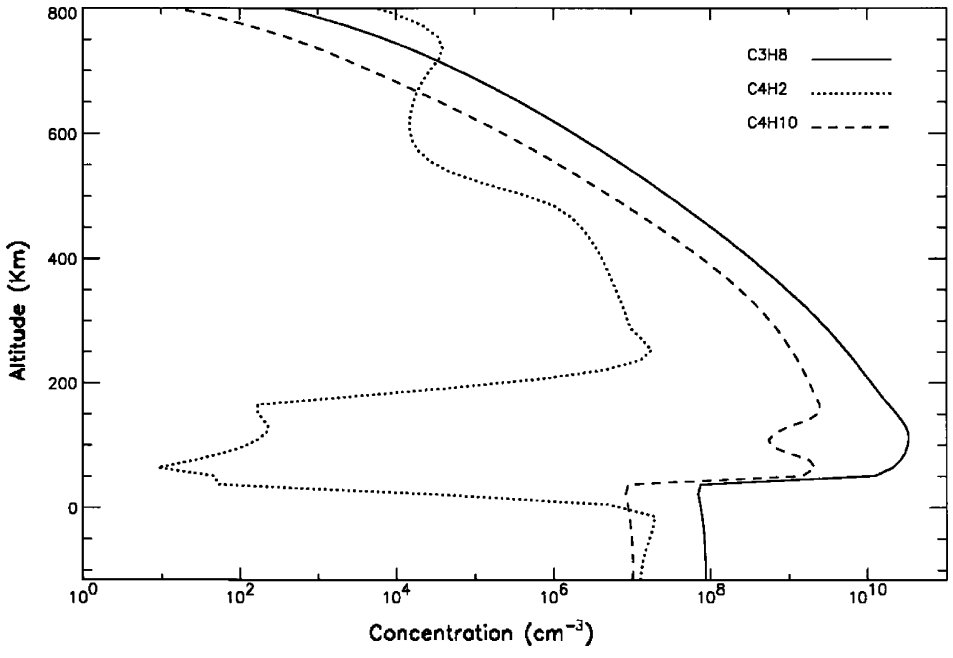

(b)

Figure 14. (a) Number density profiles for the major hydrocarbons in the atmosphere of Saturn: CH_4, C_2H_6, C_2H_4, C_2H_2. (b) Number density profiles for the major hydrocarbons in the atmosphere of Saturn: C_3H_8, C_4H_2, C_4H_{10}.

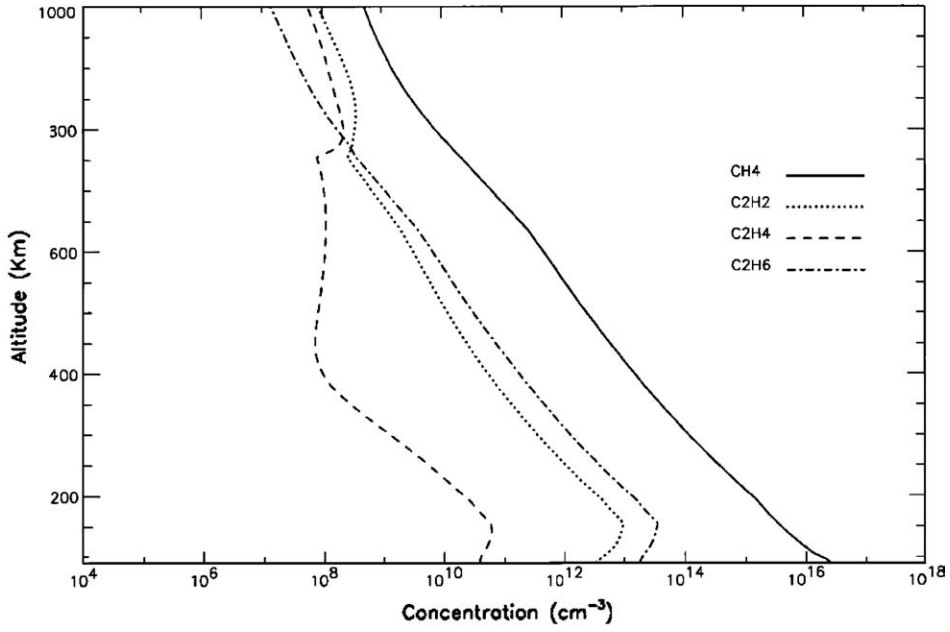

(a)

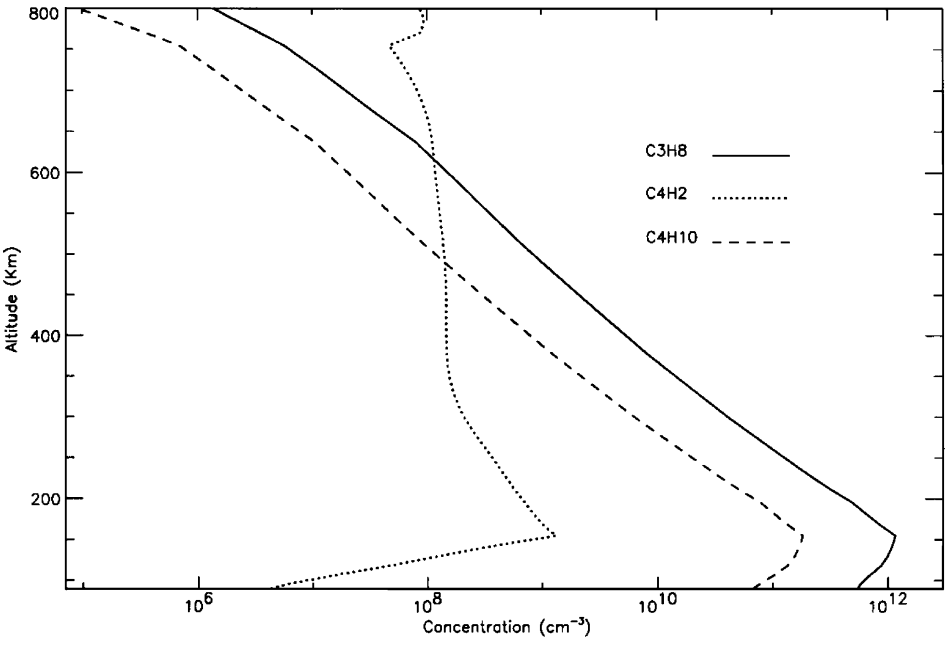

(b)

Figure 15. (a) Number density profiles for the major hydrocarbons in the atmosphere of Titan: CH_4, C_2H_6, C_2H_4, C_2H_2. (b) Number density profiles for the major hydrocarbons in the atmosphere of Titan: C_3H_8, C_4H_2, C_4H_{10}.

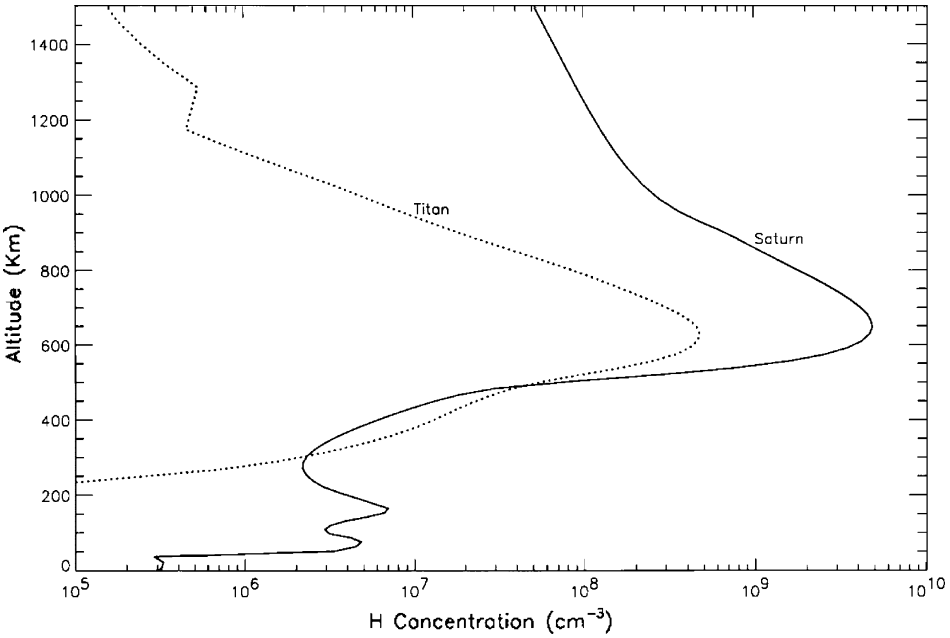

Figure 16. Number density profiles of H atoms in the atmospheres of Saturn and Titan.

is less important on Titan than on Saturn, and the methyl radicals can proceed to form higher hydrocarbons more efficiently. A careful quantitative comparison between the hydrocarbons and hydrogen from the Cassini mission is expected to reveal major new insights on the carbon chemistry in the outer solar system and to confirm or disprove some of the current models. A major puzzle is the model's failure to account for the formation of CH_3C_2H (not shown), which requires a new chemical pathway for forming this molecule. Although some of the heavy hydrocarbons are not expected to be observable by the UVIS experiment, the model provides a reference for future experiments. Also, in polar regions, the hydrocarbon concentrations may be enhanced due to auroral processes, and the model might have underestimated their concentrations.

3.3.2. *Oxygen Chemistry*

The composition of Saturn and Titan is reducing. The oxygen chemistry is entirely driven by an exogenic source, the ablation of micrometeoroids in the upper atmosphere. Figures 17 and 18 show the concentration profiles of the major oxygen species in the atmosphere of Saturn and Titan, respectively. UVIS measures O and CO directly; other species can be inferred indirectly or measured by CIRS. Although all the oxygen species are initially derived from a meteoric source, the most abundant oxygen species is not H_2O but CO. The reason is that H_2O condenses in the stratosphere and is removed from the middle atmosphere. The ultimate loss

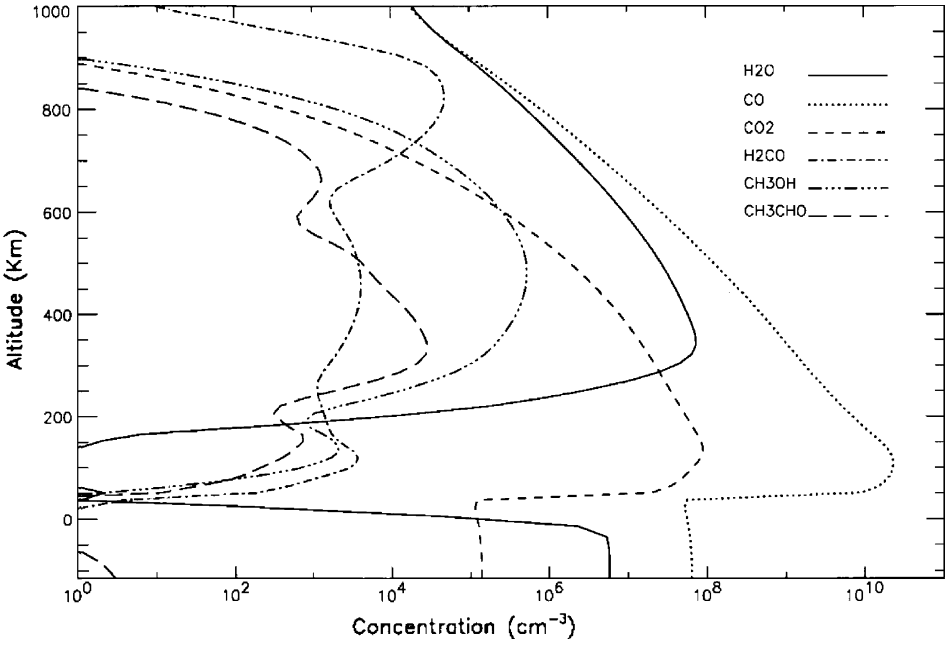

Figure 17. Number density profiles for the major oxygen species in the atmosphere of Saturn.

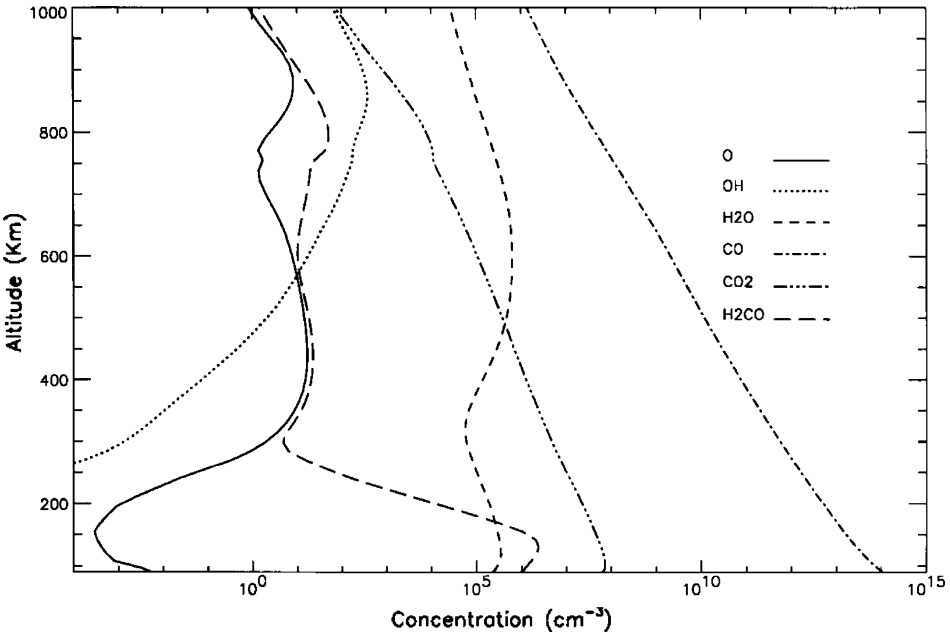

Figure 18. Number density profiles for the major oxygen species in the atmosphere of Titan.

mechanism of CO is formation of CO_2, followed by condensation at the tropopause. There is an interior sink for CO on Saturn, where CO is eventually converted to the thermodynamically stable molecules, CH_4 and H_2O. On Titan, CO is stable on the surface (like N_2). This explains the main difference between the vertical profiles of CO on Saturn and Titan. Our CO concentration for Titan is consistent with the measurements of Lutz *et al.* (1983), Muhleman *et al.* (1984), and Gurwell and Muhleman (1995). However, Marten *et al.* (1988), Hidayat *et al.* (1997), and Noll *et al.* (1996a) found significantly lower values. Since the chemical lifetime of CO on Titan is on the order of 10^9 years, we expect CO to be well mixed in the atmosphere, and there should be little change from year to year. Thus, the discrepancies between the observations are puzzling and must be resolved by future measurements. The most interesting question concerning the oxygen species on Saturn and Titan is the origin of the micrometeoroids. Are these interplanetary dust particles from the Asteroid Belt, the Kuiper Belt, the rings of Saturn; or is debris from the icy satellites transformed to exotic molecules in the atmosphere of Saturn and Titan?

3.3.3. *Nitrile Chemistry*

Figure 19 shows the nitrile compounds in the atmosphere of Titan. No nitrile compounds have been discovered on Saturn. These compounds are of great interest to

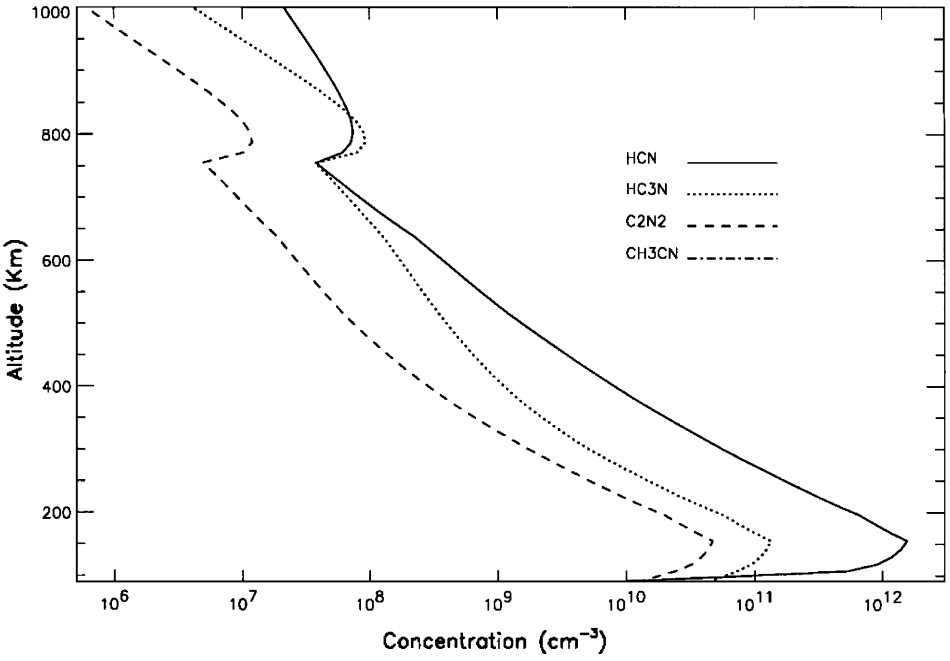

Figure 19. Number density profiles for the major nitrogen species in the atmosphere of Titan.

the origin of life as the basic constituents of amino acids and precursors to life. They are produced as a result of the photochemistry of nitrogen and hydrocarbons. Both the energy source that drives the nitrogen photochemistry and the chemical kinetics that generate and recycle these compounds are poorly understood from previous observations. For example, the abundance of CH_3CN cannot be explained by chemistry based on measured kinetics.

The model of Lara *et al*. (1996) is based on the reaction:

$$CN + CH_4 \rightarrow CH_3 + HCN \tag{9}$$

$$CN + CH_4 \rightarrow CH_3CN + H \tag{10}$$

While branch (9) is well known, branch (10) has never been measured. Detailed observations of the altitude profile of CH_3CN in the future would provide a test of this hypothesis.

In summary, the Cassini UVIS observations will result in major advances in our understanding of the upper atmospheres of Saturn and Titan:

(1) The temperature of the thermosphere and the heating mechanism responsible for maintaining the high temperature on Saturn.
(2) The eddy mixing in the atmospheres of Saturn and Titan; comparison of an atmosphere without a surface and a thick satellite atmosphere with surface and possibly ocean.
(3) The efficiency of organic synthesis in an H_2 dominated atmosphere versus that in an N_2 dominated atmosphere.
(4) The impact of hydrogen escape at the upper boundary on atmospheric chemistry.
(5) The magnitude and fate of the influx of oxygen in the ablation of micrometeoroids in the atmospheres of Saturn and Titan.
(6) The chemical pathways leading to the formation of Danielson-Axel aerosols in the atmospheres of Saturn and Titan.

4. Clouds and Aerosols

4.1. Stratospheric Aerosols

The study of aerosols touches on many facets of atmospheric science. Aerosols are one of the end products of chemistry in the high atmosphere initiated by the breakup of molecules by photolysis and by charged particle bombardment. Charged particle bombardment is thought to be especially important in auroral regions. Aerosols absorb solar radiation and thereby play a role in the energy balance and meridional circulation of the stratosphere. UV wavelengths are more sensitive than longer wavelengths to small particles, which have a long residence time in the stratosphere and can serve as tracers of the circulation and horizontal eddy transport. Observations by UVIS will lead to detailed knowledge of their UV optical properties

and vertical distribution, which are necessary to estimate solar heating, and can be used along with observations of infrared cooling and heating to derive the mean meridional circulation, as West *et al*. (1992) have done for Jupiter's stratosphere. These observations are also necessary to derive aerosol number density, size, shape, and refractive index, which in turn serve to constrain aerosol/chemical life-cycle and microphysical models.

Ultraviolet wavelengths remotely sense the stratospheres of Saturn and Titan. Molecular scattering by H_2 and He provides enough opacity to establish vertical optical depth 1 at 37 mbar at 190 nm wavelength, decreasing to lower pressure approximately as λ^{-4}. Additional opacity due to gas (mostly hydrocarbons, see Section 3) and aerosol constituents will push this level to even lower pressures, especially near the poles, which are considerably darkened. In Titan's stratosphere, an optically thick aerosol haze dominates the opacity at wavelengths down to 180 nm and causes Titan's geometric albedo to be remarkably low (0.02 from 180 to 220 nm, McGrath *et al*., 1998).

4.2. Saturn

Saturn's banded appearance is the result of cloud and aerosol particles, which are transported by the zonal wind structure. As on Jupiter, the polar and low-latitude regions are distinctly different. Equatorward of the transition region, the atmosphere is moderately absorbing, but at higher latitudes the concentration of absorbers is much greater. This difference may be attributable to the strong contribution that auroral energy deposition makes to aerosol formation in the auroral zones, coupled with a dynamical confining mechanism (such as a zonal jet at the transition latitude), which inhibits particle transport to lower latitudes. Auroral processes have been implicated for aerosol formation on Saturn ever since the Voyager 2 photopolarimeter experiment showed UV absorbers to be concentrated at high latitude (Lane *et al*., 1982; Pryor and Hord, 1991). Jaffel *et al*. (1995) discovered an auroral dark oval in the northern polar region. They considered this to be strong evidence for an auroral connection to UV haze production.

Previous work on Saturn's aerosols and their connection to auroral processes leaves us with a number of questions. What is the nature of the dark feature associated with the aurora? Does it serve as a tracer for recent (within hours) aerosol formation, or does it reflect processes operating over longer time scales? At what altitudes do the aerosols begin to form? What dynamical process produces the sharp transition region? Can we see longitudinal contrasts over short spatial scales, and can they be exploited to reveal the nature of the zonal wind field at mbar pressures in the polar stratosphere? Are there variations over short or long time scales, and what do they imply? What are the sizes and shapes of the particles, and what is the nature of the microphysical processes that govern these parameters? What are the compositions of the particles at high and low latitude?

The UVIS instrument will provide information uniquely suited to addressing these questions. It will supply images of Saturn at many wavelengths between about 150 and 190 nm, which will be used to study the morphology of the banded structure and of the illuminated polar region. These images will have several advantages compared to what is obtainable from earth orbit, including better viewing angles during high-inclination orbits, better signal-to-noise ratio, frequent temporal coverage over a 4-year period, and phase angle coverage. Phase angle coverage provides information on the scattering phase function of the particles, which is diagnostic of the particle size distribution. Together with information at other wavelengths from other instruments, it will help constrain particle shape and the imaginary part of the refractive index (which is diagnostic of composition).

Solar and stellar occultations will be used to measure the vertical profile of aerosol and gas opacity at the highest altitudes (pressure less than about 0.2 mbar). Solar occultations (with EUV only) provide EUV signal but are rare (at most a few during the mission), and the spatial resolution is limited by the angular size of the sun's disk as projected on the limb. These provide direct measurements of the atomic hydrogen density and the thermospheric temperature. One or more stellar occultation events (primarily FUV) are expected for every orbit, providing modest latitudinal coverage and high spatial resolution in the vertical. Opportunities to do vertical profiling in and near the auroral region will be particularly interesting, since the altitudes probed coincide with the location of auroral energy deposition. In addition to aerosol and gas-opacity profiles, these occultation measurements will provide temperature information over one or two scale heights. An estimate of zonal winds at low pressure is possible within a limited latitude range if the latitudinal density of occultations is sufficient to derive isobaric slopes.

4.3. TITAN

The importance of aerosols to atmospheric physics and chemistry is nowhere more evident than on Titan, and many papers in recent scientific literature have concerned themselves with Titan aerosols. Titan's atmosphere contains mostly nitrogen with trace amounts of hydrocarbons, mostly methane. Destruction of methane by photolysis (Yung *et al*., 1984) and by charged particle bombardment from Saturn's magnetosphere, the solar wind, and high-energy cosmic rays leads to the production of a plethora of hydrocarbons and nitriles (see Section 3). Through a process as yet too complex to model accurately, these molecules lead to the formation of small haze particles high above the surface (in the altitude range 350 to 600 km). Several laboratory studies and theoretical treatments have revealed likely chemical pathways and products in this process (Yung *et al*., 1984; Thompson *et al*., 1994; Devanssay *et al*., 1995; Zweir and Allen, 1996; McKay, 1996; Clarke and Ferris, 1997).

Refractive indices of the particles derived from studies of Titan's geometric albedo are within a factor of 2 of those produced in the laboratory work of Khare *et al*. (1984). The particles do not absorb much at red wavelengths but absorb strongly at UV wavelengths. The particles that formed in several of the laboratory studies were aggregates of small spheres (Bar-Nun *et al.*, 1988; Scattergood *et al*., 1992). Aggregate particles can account for the combination of modest forward scattering (near 160° phase angle) and high linear polarization (near 90° phase angle) produced by Titan's haze (West and Smith, 1991; Lemmon, 1994; Rannou *et al*., 1997).

Conventional aerosol microphysical models for Titan assumed that the particles are spheres (e.g., Toon *et al*., 1992). Tomasko and Smith (1982) proposed a vertically inhomogeneous model with an optically thin layer of larger particles at the top of the atmosphere to account for the combination of forward scattering and linear polarization. Toon *et al*. (1992) showed how that scenario could be supported with a microphysical model having upwelling at some latitudes. They simultaneously account for the detached haze layer seen in Voyager images (Rages and Pollack, 1983). Haze morphology in the polar region as seen in Voyager images has considerable structure, indicating the importance of atmospheric dynamics in aerosol formation and transport.

More recent models of haze microphysics have emphasized the aggregation process. This work has been carried out mostly by Cabane *et al*. (1993), Chassefiere and Cabane (1995), and Rannou *et al*. (1997). These models have become more sophisticated with time, attempting to account for details of the haze vertical structure as well as the fractal dimension of the particles.

Yet another important facet of Titan aerosol science is the observed north/south contrast and seasonal variation. Karkoschka and Lorenz (1997) used images of Titan's shadow on Saturn to derive a north/south difference in altitude of the optical limb of the planet, which is close to zero at 337 nm wavelength but is 130 km at 954 nm. This implies a hemispheric asymmetry in aerosol size (0.3 μm mean radius in the north compared to 0.1 μm mean radius in the south). We still don't have a good understanding of the highly coupled chemical/microphysical/ radiative/dynamical processes that produce the observed asymmetries and their variations with time.

Observations by the UVIS instrument will provide unique and important information to help sort out current questions about Titan aerosols. Maps of Titan's reflectivity at many latitudes and phase angles at UV wavelengths will put new constraints on the size distributions and shapes of particles as a function of latitude. At close range (within 20,000 km of Titan), imaging along the limb will resolve structure whose scale height is much smaller (20 km or less) than the scale height of the gas. Because ultraviolet wavelengths are sensitive to small particles, the UVIS experiment will provide critical information on the aerosol formation region (300 to 600 km altitude). Solar occultations at Titan can resolve subscale-height structure and provide important information on gas and aerosol opacity at high altitude. Multiple stellar occultations will allow detailed vertical profiling of gas and aerosols at many latitudes down to an altitude of approximately 350 km.

In concert with Cassini images and IR spectroscopy, this will allow a complete picture of Titan's stratosphere, which can be linked to the Huygens probe results at lower altitudes from the Descent Imager/Spectral Radiometer (DISR) experiment.

5. Thermospheres and Exospheres

5.1. Introduction

The unexpectedly high thermospheric temperatures of the giant planets are an unsolved puzzle. Unlike the terrestrial planets, we cannot explain their high temperatures (see Figure 20). UVIS can measure the various heating mechanisms by their direct and indirect effects on UV thermospheric emissions.

5.2. Saturn

5.2.1. *Saturn's Aurora*

The Voyager UVS obtained limited information on Saturn's aurora, which showed strong intensity variations in both north and south ovals (Sandel and Broadfoot, 1981; cf. Broadfoot *et al*., 1981; Sandel *et al*., 1982). More recent measurements

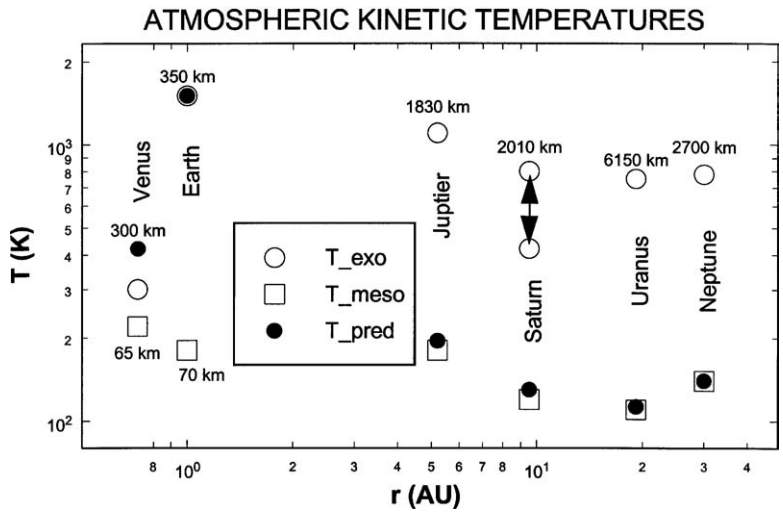

Figure 20. Kinetic temperatures of the atmospheres of the giant outer planets compared to the Earth and Venus. Open circles are the temperatures measured at the tops of the thermospheres (exobase; note range for Saturn). Filled circles are the temperatures predicted through model calculations. The modeled exobase temperatures for the outer planets are based on solar radiation input and the known thermal transfer properties of H_2. Open squares are the mesospheric temperatures. Altitudes of the exobase are indicated on the plot.

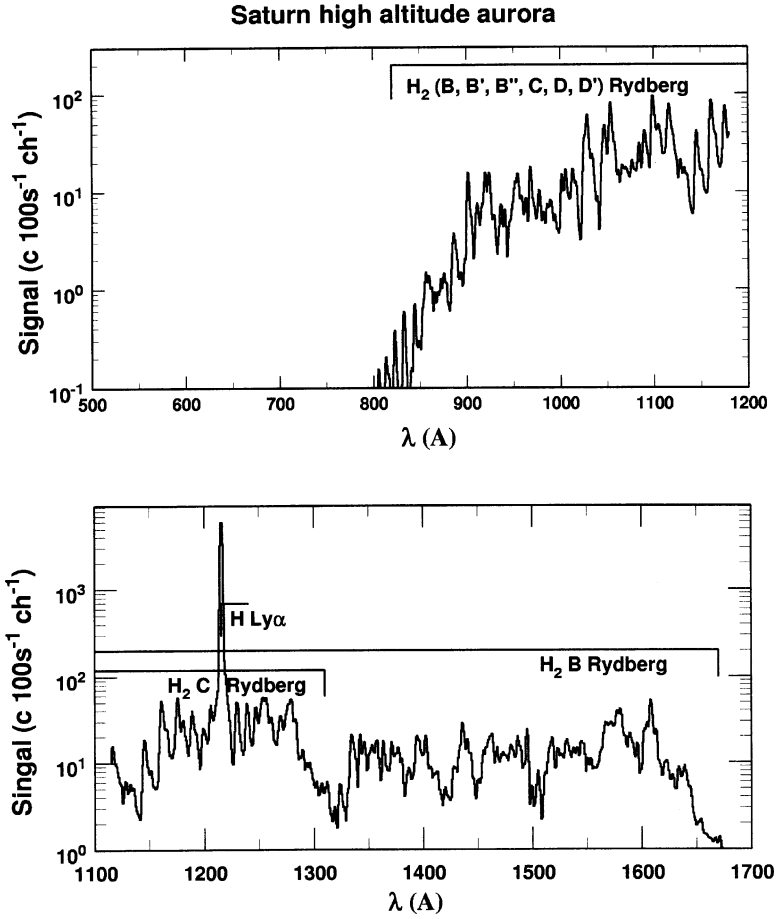

Figure 21. Model synthesis of high altitude Saturn auroral spectra in the UVIS EUV and FUV channels, showing H_2 bands and H emissions excited by soft electron precipitation. A brightness of 10 kR is assumed.

with the HST's WFPC2 and STIS (Trauger *et al.*, 1998) show temporal, longitudinal, and local time effects. The UVS data showed that much of the emissions come from the high thermosphere, implying very soft primary particles together with brighter, spatially confined 'hot spots' whose spectra are similar to those of Jovian aurorae and therefore imply primaries with sufficient energy to penetrate to the hydrocarbon homopause. The variations, the differences from Jovian aurorae, and the evidence that neutral gases dominate Saturn's magnetosphere indicate very significant dissimilarities between Saturnian and Jovian processes. The study of Saturn's aurora by UVIS will further explore these differences and should greatly advance our understanding of the Saturnian phenomenae. A model of the UVIS response to a 10 kR aurora is shown in Figure 21.

5.2.2. *Saturn's Airglow*
The H_2 emissions in Saturn's dayglow show a spectrum very similar to that of its high-altitude 'soft' aurora (and to that of Jupiter's dayglow (Sandel *et al*., 1982; Shemansky, 1985; Shemansky and Ajello, 1983)). The H emissions are relatively stronger than in the aurora, suggesting a larger H/H_2 ratio or a substantial difference in source function. Although the Voyager UVS observations were affected by the weaker signal and the presence of the rings and their shadow, the Saturnian dayglow clearly differs from the Jupiter dayglow. Dawn is twice as bright as dusk, and the H Lyman-α and H_2 bands show limb-brightening at dawn, whereas Jupiter shows limb-darkening in H Lyman-α and H_2 emissions at both dawn and dusk. Saturn does not show Jupiter's Lyman-α 'bulge' in longitude. Limb profiles at Saturn showed airglow scale heights five times larger than that of neutral H_2, indicating a high-altitude source for the airglow other than solar radiation. Precipitation of soft electrons could explain the airglow and, by dissociating H_2, provide both a source of thermospheric heating and a source of the observed magnetospheric H. A model of the UVIS response to the dayglow is shown in Figure 22.

5.2.3. *Occultation Measurements of Thermospheric Structure*
Solar and stellar occultations provide composition and temperature information throughout the thermosphere. Solar occultations below 912 Å yield exospheric temperature and both H and H_2 profiles in the upper thermosphere. At lower altitudes, where the angular size of the Sun exceeds the relevant scale heights, stellar occultations yield temperature and the identity and vertical distribution of absorbing hydrocarbons around the homopause. Analysis of Voyager occultation data also yielded the vertical flux of H and the eddy diffusion coefficient (Smith *et al*., 1983; Festou and Atreya, 1982).

5.3. Titan

Titan, like Triton and Pluto, has an atmosphere dominated by N_2, and CH_4 is the most abundant trace gas. Their atmospheres derive from the slow release of CH_4 and NH_3 from clathrates in the interior, with the NH_3 photolyzing to produce N_2 (Atreya *et al*., 1978), and the delivery of volatiles by cometary impact (Zahnle and Dones, 1992).

5.3.1. *Thermospheric Emissions and Structure*
Titan's atmosphere shows FUV and EUV emissions from N_2, N, N^+, and H, which are detectable on the night side and much brighter in sunlight. The excitation mechanisms involve magnetospheric-particle precipitation and photoelectrons, perhaps accelerated by internal processes (Hall *et al*., 1992). The particle deposition may also produce both heating in and atom escape from the exobase region. Voyager spectra of the $N_2C'4$-X system are unaffected by predissociation, implying generation at the exobase (Shemansky *et al*., 1995) and hence a flux of soft electrons.

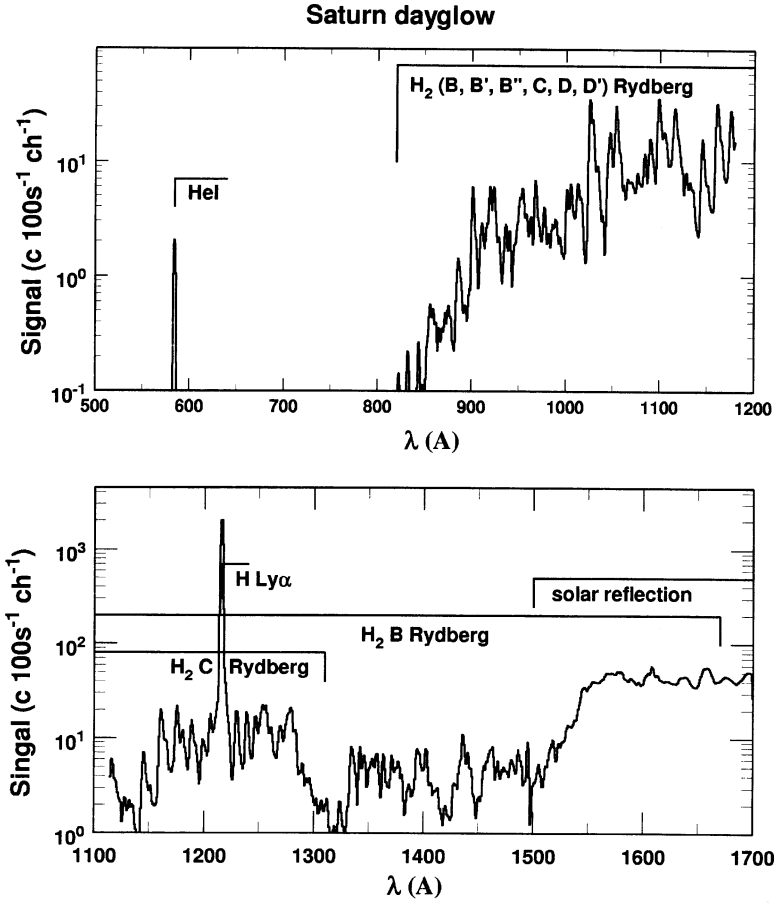

Figure 22. Model synthesis of Saturn dayglow spectra in the UVIS EUV and FUV channels showing soft-electron excited H_2 and H. The long wavelength region is dominated by the reflection of solar radiation. A brightness of 1.0 kR for the H_2 bands is assumed, matching the value obtained by the Voyager UVS experiment.

These electrons would also dissociate N_2 and any H_2 present; heating and escaping atoms would result.

5.3.2. *Occultation Measurements of Thermospheric Structure*

Voyager UVS occultation data analyzed by Smith *et al.* (1982) at several wavelengths (Figure 23) yielded temperature and composition information for altitudes between 400 and 1200 km. At dusk near the equator, the exospheric temperature was 186 K. Photolytic conversion of CH_4 to C_2H_2 was seen above 800 km, and two absorbing haze layers were seen. The lower layer (at 375 km) appeared uniform, which was confirmed by the Voyager cameras (Rages and Pollack, 1983). The upper layer (700 to 1100 km), presumably composed of polyacetylenes, differed

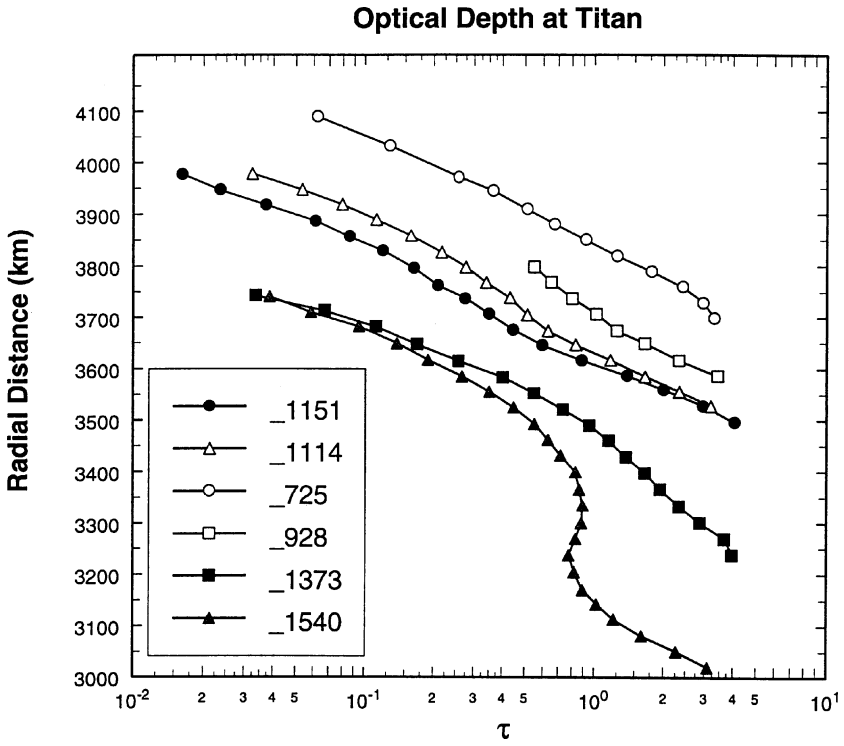

Figure 23. Voyager 1 UVS ingress (2.74°N) occultation measurements of optical depth at various indicated wavelengths as a function of radial distance from the center of Titan (after Smith, *et al.*, 1982).

between ingress and egress. Other nonuniformities in temperature and composition have been reported by the Voyager IRIS (Coustenis, 1992). The Cassini UVIS, with much better resolution and sensitivity than the Voyager UVS, should provide information to within 100 km of the radio occultation limit of 200 km.

5.4. MAGNETOSPHERE

Both Saturn and Titan may supply neutrals to the magnetosphere. In any case, there is compelling evidence that considerable amounts of water are supplied by sputtering from ices in the system. The Voyager UVS detected H at out to 20 Rs, with a peak density of 100 cm^{-3} and extending 8 Rs above and below the equatorial plane. HST has detected OH at 4.5 and 6 Rs, with a null result at 8 Rs. There are theoretical grounds for expecting O in amounts similar to OH. Other sputtering products may be present in quantities detectable by UVIS, in addition to the H and O. The large neutral/ion ratios will have a large effect on magnetospheric energetics and structure.

5.5. JUPITER

Cassini will fly past Jupiter in December 2000, presenting the opportunity to examine questions raised by earlier observations at similar wavelengths (the Voyager UVS, the Galileo UVS and EUV, the IUE, the HUT, and the EUVE). The UVIS combination of sensitivity, resolution, wavelength coverage, imaging capability, and potential for extended synoptic coverage in many ways exceeds the sum of these earlier instruments.

5.5.1. *Jupiter's Aurora*

The auroral spectrum consists of emissions from H_2 and H showing the effects of self-absorption by H_2 and of absorption by CH_4, C_2H_2, and perhaps C_2H_6. X-rays have been detected (Waite *et al*., 1994), perhaps originating from the precipitation of heavy magnetospheric ions (Cravens *et al*., 1995; Gladstone *et al*., 1998). Information on the energy of the precipitating particles can be obtained from the absorption features and the relative strengths of the Lyman series of H. Galileo and HST images have shown the auroral oval to be narrow (200 km) and structured, with variable emissions from inside the oval in the dusk sector. System III longitudinal dependence is well studied.

5.5.2. *Jupiter's Airglow*

Airglow emissions from H, H_2, and He have been detected (Shemansky, 1985; Feldman *et al*., 1993). They are all limb-darkened, as is the reflected solar continuum at 166 Å. X-rays from an unknown excitation process have been measured at low latitudes (Gladstone *et al*., 1998). UVIS, with its superior resolution and its spectral coverage, is well suited to throw light on the excitation and absorption mechanisms. It may also provide a resolution of the controversy surrounding the interpretation of the H_2 emissions.

5.5.3. *Io's Plasma Torus*

Detailed observations of the torus's radiant output (90% of which falls within UVIS's range), ion composition, electron temperature, and structure will provide new information on its energy budget to elucidate its energy sources. UVIS may also detect the O and S atoms escaping from the torus and the Jovian system. Figure 24 compares a Galileo UVS/EUV spectrum at 35 to 40 Å resolution with a model of the UVIS EUV response to torus emission at 2.4 Å resolution.

5.6. SUMMARY

The Cassini UVIS will bring to bear on the Saturn system considerably greater capabilities than possessed by the Voyager and Galileo UVS/EUV instruments. The long time scale of the Cassini tour will provide opportunities for multiple spectral images and solar and stellar occultations. These will provide the data to

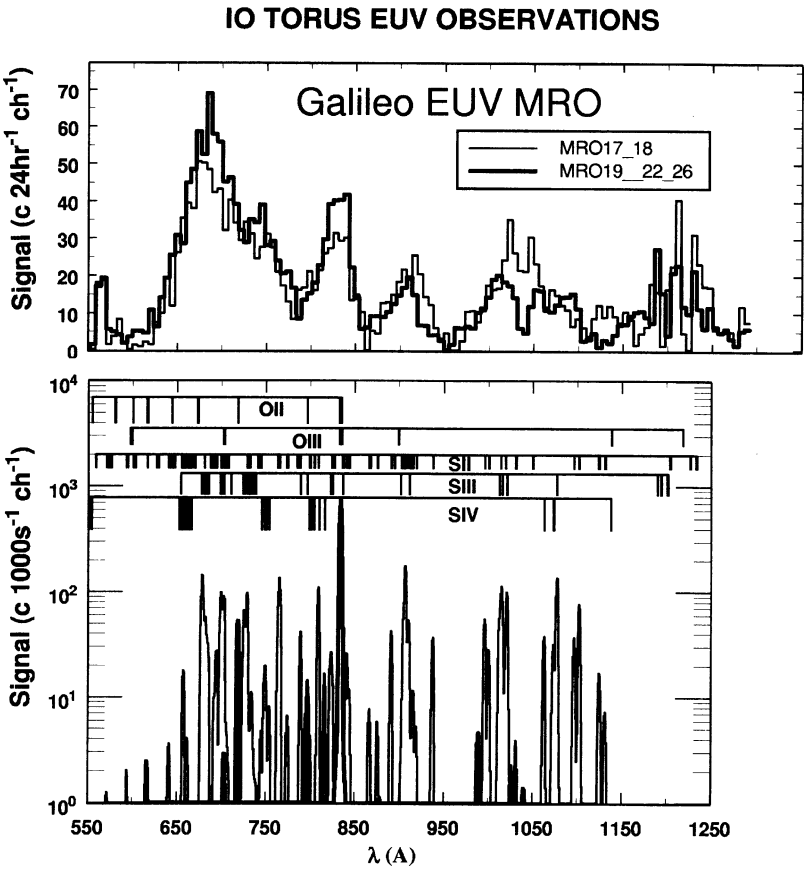

Figure 24. Comparison of modeled UVIS spectrum of Io plasma torus with Galileo observation. The predicted UVIS spectrum at 2.4 Å resolution obtains higher total signal counts in 1000 s than those obtained by the Galileo EUV instrument in 24 h, at a resolution of 40 Å.

examine and explain the thermospheric energy balance and to elucidate the supply of neutrals to Saturn's unique magnetosphere.

6. Icy Satellite Surfaces and Exospheres

Saturn's entourage of icy satellites is an important target for the Cassini mission. Most of what we know about Phoebe, Iapetus, Hyperion, Rhea, Dione, Tethys, Enceladus, Mimas, Janus, and Epimetheus (to name just the larger moons) dates from the Voyager mission. The distance of the flybys and limited capability of the Voyager ultraviolet spectrometer leave much for the Cassini UVIS to discover.

The moons of Saturn, whose orbits are within Titan's orbit (except Hyperion, Iapetus, and Phoebe), are embedded in Saturn's magnetosphere. Composed primarily of water ice, they are too small to retain the thick atmosphere of their large sibling,

Titan. Their surfaces bear the signature, both in terms of radiation damage and evolved chemistry, of long exposure to Saturn's charged particle environment. New discoveries on the Galilean satellites of oxygen chemistry driven by charged-particle bombardment and UV photolysis of water ice are relevant to Saturn's moons, also. Molecules sputtered from the icy satellite surfaces may form tenuous atmospheres, and they are a source of matter to Saturn's magnetosphere.

With UVIS we will use the interaction between the satellite surface and its magnetospheric environs to study three key areas of icy satellite science: (1) surface age and evolution, (2) surface composition and chemistry, and (3) tenuous atmospheres/exospheres.

6.1. Surface Age and Evolution

Voyager images suggest complex thermal and geologic histories: for example, clear regional differences in surface age are visible in the Voyager images of Enceladus. Enceladus is speculated to be the source of Saturn's E ring, possibly implying the existence of some sort of geologic activity supplying particles. Intriguing low-resolution images of 'wispy terrain' on Rhea and Dione also suggest regional units that have experienced very different thermal histories than are visible in high-resolution images of cratered regions of their surfaces (Smith *et al.*, 1982). Our goal with UVIS will be to establish the exposure history of surface units by measuring their UV albedo, thus addressing regional age.

Saturn's icy satellites, which orbit within Saturn's magnetosphere, experience the impact of energetic particles onto their surfaces; this bombardment can eject atoms and molecules from the surfaces, affect surface microstructure, and cause chemical alteration (e.g., Cheng *et al.*, 1986; Johnson and Quickenden, 1997; Delitsy and Lane, 1998). Surface UV albedo is affected by radiation darkening and surface chemistry and thus will vary with the amount of time; a unit has been exposed to the magnetosphere's radiation and high energy particles.

Leading-side versus trailing-side asymmetries are to be expected. Bound magnetospheric plasma orbits faster than the satellites and thus impacts their surface on the trailing side. The leading sides of Dione and Rhea are indeed brighter than their trailing sides (Nelson and Lane, 1987).

The Galileo discovery at Jupiter that Ganymede certainly, and possibly Europa and Callisto, have internally generated fields and possess their own magnetospheres (Kivelson *et al.*, 1997) is also relevant to our investigation of Saturn's icy satellites. A magnetosphere will protect the satellite surface from Saturn's plasma bombardment. The structure of the satellite's magnetosphere may affect the geographic distribution of radiation damage by focusing radiation along open field lines (Johnson, 1997). In this case, rather than being able to determine relative surface ages, we may be able to study the structure of the moon's own magnetosphere.

The fact that the orbits of Hyperion, Iapetus, and Phoebe are well outside Saturn's magnetosphere, except when they are in the portion of their orbits that carries them through Saturn's magnetotail, gives us the opportunity to compare surfaces with quite different exposure levels.

The Cassini UVIS will acquire full disk albedo maps of each of the Saturnian satellites and spatially resolved spectra for most of the satellites. We will assemble the albedo map from observations acquired every 15° of longitude and 10° of latitude, resolution permitting, for each of the major moons. Three factors determine exposure history: the existence of an internal magnetosphere, the structure of the Saturn magnetosphere (e.g., leading- vs. trailing side bombardment), and the amount of time a surface unit has been exposed (which depends on the geologic history). In order to separate these causes, UVIS data maps will be correlated with imaging data to quantify the relationship between UV darkening and surface age. Cassini magnetometer data for close flybys may determine the existence of internal magnetospheres. Disk-resolved UV spectra have been used quite successfully by the Galileo Ultraviolet Spectrometer (UVS) Team to carry out similar investigations (Hendrix *et al*., 1998).

In addition to relative age, surface evolution can be investigated by looking at surface microstructure via the phase function. Surface scattering properties are determined by the surface microstructure and large-scale roughness. The phase function will be different depending on whether the surface is smooth or structured at the scale of the wavelength being investigated, providing insight into the evolution of the regolith. One fascinating Voyager result is that in spite of the very different ages and appearance of different regions on Enceladus, the albedo, color, and photometric function properties are uniform, suggesting the possibility of a thin, ubiquitous layer of geologically fresh frost (Buratti and Veverka, 1984; Veverka *et al*., 1986; Buratti, 1988).

Cassini will view Enceladus at ±0.01° phase angle, allowing us to measure the opposition effect, which in turn yields surface porosity. We will acquire phase curves for all of the Saturnian satellites, from 0° (Enceladus only) or 5° (most of the other satellites) to 160°.

6.2. Surface Composition and Chemistry

The bulk composition of the Saturnian satellites is predominantly water ice. Their surfaces are nearly pure water ice (Clark *et al*., 1984), but with enough compositional or morphological differences to cause their spectra and UV/IR color ratios to be significantly different (Clark *et al*., 1986; Nelson and Lane, 1987) from each other and from the Jovian and Uranian satellite families. In spite of these differences, we use the Jovian satellites as predictors of phenomena we may expect to find in the Saturnian system, adjusted for the colder temperatures.

Investigation of photolysis and radiolysis of water ice is currently a very active area of research, propelled by recent Galileo results, earth-based observations,

and laboratory work. UV radiation dissociates H_2O into H and OH, and H_2. H_2, O, and O_2 are produced from H and OH. H and H_2 are quickly lost to thermal escape. The flux of atomic hydrogen escaping from Ganymede has been measured by the Galileo UVS (Barth *et al*., 1997). O and O_2 have been detected at Europa and Ganymede (Hall *et al*., 1995; Spencer *et al*., 1995; Calvin *et al*., 1996; Saur *et al*., 1998); thus, we might expect to detect these species at the Saturnian satellites. Reactions powered by solar UV ice photolysis have significant energy available but only affect the top tens of monolayers of the satellite surface. Plasma bombardment penetrates deeper, and the products may stay in the solid surface long enough to participate in other reactions, for example, providing the possibility for O_2 to form O_3. Spectral absorption suggestive of ozone has been detected by the Galileo UVS on Ganymede (Hendrix *et al*., 1999) and by the Hubble Space Telescope on Ganymede, Rhea, and Dione (Noll *et al*., 1996b; Noll *et al*., 1997). Laboratory results are not entirely consistent with Galilean satellite observations, however (Vidal *et al*., 1997 and Baragiola and Bahr, 1998), so being able to compare oxygen chemistry at a variety of temperatures and radiation environments will help in understanding the processes.

Use of the ultraviolet portion of the spectrum for compositional studies of a surface is difficult, since few solids have features in the UV. If, however, component atoms and molecules are sputtered or sublimated from the surface, vapor phase spectral features may be detectable. With UVIS, we will look in particular for the spectral signature of O, N, N_2, and CO as indicators of CH_4, acetylene, ammonia ice, and water ice-oxygen chemistry. An ammonia-water ice composition that would have a lower melting point than pure water has been proposed to explain the young geology on Enceladus (Stevenson, 1982; Squyres *et al*., 1983). UVIS compositional data may give us insight into whether endogenic or exogenic processes have been responsible for the state of the surfaces of Iapetus and Phoebe. Comparison of compositional differences from one Saturnian satellite to the next may provide additional perspective on the formation of the Saturnian satellite system.

6.3. Tenuous Atmospheres and Exospheres

It is known that molecules are being sputtered from the surfaces of the Saturnian satellites from the distribution of neutrals and ions in Saturn's magnetosphere (Shemansky *et al*., 1993). It is possible that vapor pressure atmospheres of constituents more volatile than water ice exist. Regardless of how these tenuous atmospheres are produced, they are more properly regarded as exospheres, since the atmospheric density is expected to be extremely low. In the following paragraphs *atmosphere* and *exosphere* are used interchangeably.

UVIS objectives are to address the following questions:

(1) Do Saturn's icy satellites possess extremely tenuous atmospheres due to sputtering or seasonal sublimation?

(2) What is the composition of these atmospheres? Can we identify trace constituents in their vapor phase, which would support the hypothesis that the satellites' water ice surfaces contain some amount of methane clathrates or NH_3 hydrate?
(3) Do we see any evidence of seasonal volatile transport? Can we detect and measure the flux of escaping atomic H produced by photolysis and sputtering of water ice?
(4) Can we identify (on Enceladus, in particular) evidence for transient or localized volatiles in the atmosphere associated with eruptive activity such as geysers? Are the constituents of these plumes particulate or gas?

We will employ three different observational techniques to address these questions: limb drifts to search for scattered light, stellar occultations to detect atmospheric absorptions, and integrations on the night sides to see atmospheric emission.

Given the low surface temperatures of the Saturnian satellites, a vapor pressure equilibrium water atmosphere is not to be expected at detectable levels using limb drifts. A sputtered water atmosphere may be detectable (see Cheng *et al*., 1986 for an excellent description of sputtering- vs. sublimation-produced atmospheres). A primary goal is to search for more volatile trace constituents such as NH_3 or CH_4, implicated to exist in Saturnian satellite surface ices, or N_2, the product of photolyzed NH_3. On Titan, the temperature and pressure of the solar nebula at Saturn could have allowed as much as 15% NH_3 or CH_4 to be trapped in water ice as hydrates or clathrates during satellite formation (Lunine and Stevenson, 1985; Stevenson, 1991). Clathrates would end up primarily near the surface by subsequent differentiation of the satellite. Massive Titan, with its substantial gravity relative to the icy satellites, is able to retain its volatiles as a substantial atmosphere. With the same source surface ices but the much lower gravitational fields of the icy satellites, we may find very much thinner atmospheres. Rough use of Raoult's law predicts that N_2 produced by photolysis of NH_3 will be easily detectable by UVIS at the surface ice temperatures of the Saturnian satellites, with CH_4 almost as easily detectable.

Stellar occultations provide a powerful technique for the study of planetary atmospheres (e.g., Smith and Hunten, 1990). The Voyager UVS was able to place an upper limit on the surface pressure of a hypothetical Ganymede atmosphere of 10^{-11} bar by observing the occultation of Kappa Centauri, a moderately bright UV star (Broadfoot *et al*., 1979) and assuming that a 10% extinction of the starlight would have been detectable by UVS. With the higher sensitivity of the Cassini UVIS instrument, and given adequate stellar occultation opportunities (i.e., star type, brightness), UVIS will be able to do at least as well at the Saturnian satellites.

The signature of oxygen emission excited by electron impact has been detected at Europa (Hall *et al*., 1995) at 130.4 and 135.6 nm. Since we expect similar processes of photolysis and radiolysis of ice to produce O and O_2 on Saturn's other satellites, we will search their night sides for this airglow.

7. Deuterium in the Saturn System

7.1. Scientific Background: The Significance of D/H in the Solar System

Most (perhaps all) of the deuterium in the universe was produced shortly after the big bang, when temperatures were high enough to allow its formation. As deuterium finds its way into stars, it is destroyed in the second step of the proton-proton chain (${}^2_1\mathrm{H} + {}^1_1\mathrm{H} \rightarrow {}^3_2\mathrm{He} + \gamma$). This process, called astration, depletes the universe of deuterium as it cycles its way through star formation, astration, and interstellar injection. As a consequence, the ratio of deuterium to hydrogen in the interstellar medium (ISM) has been decreasing since the universe began and currently has a value of 2×10^{-5} (McCullough, 1992). The mass difference between the two atoms causes different vibrational and rotational energies in H_2 and D_2 molecules, different diffusion rates, different thermodynamic characteristics, and slightly different electronic energies. For these reasons, the measurement and interpretation of these isotopic effects yield important clues to understanding the processes involved in the formation and evolution of the planets.

Measurements of the deuterium-to-hydrogen ratio (D/H) in the solar system reveal two distinct reservoirs of deuterium, both of which are believed to predate the solar system itself (Owen *et al*., 1986). The first reservoir is deuterium enriched relative to the second and includes the Earth, Mars, Uranus, Neptune, Titan, and cometary material. The second reservoir consists of Jupiter, Saturn, and the Sun. The general explanation for the differences in D/H between these two reservoirs lies in the theory of their formation (Owen, 1994). During the formation of the solar system, the cold, deuterium-enriched (D/H $\sim 2 \times 10^{-4}$) molecular clouds (Geiss and Reeves, 1981) in the interstellar medium accreted to form the cores of the planets and other solid bodies. These icy/rocky cores outgassed deuterium (generally in the form of deuterated methane) in a process that preserved the deuterium enrichment (Owen, 1994).

The D/H ratio of the second reservoir (Jupiter, Saturn, and the Sun, D/H $\sim 2 \times 10^{-5}$) closely matches that of the interstellar medium and the solar nebula (Owen, 1994). If the cores of the accreting material became large enough, they captured gas from the solar nebula and assumed the corresponding D/H ratio. Because Jupiter and Saturn have a low ratio of core mass to total mass (around 0.03 to 0.06 for Jupiter and 0.11 to 0.22 for Saturn (Owen, 1994)), they are believed to be primarily derived from the main reservoir of gas in the proto-solar nebula. Measurements of Jovian and Saturnian D/H support this theory.

To date, measurements of D/H in the atmospheres of the outer planets have been made by measuring deuterated molecules from Earth-based telescopes and by direct measurements of Jupiter by the Galileo probe mass spectrometer (Mahaffy *et al*., 1998) (Table V). A comparison of Saturn hydrogen Lyman-α intensities from Voyager 1 and 2 with IUE measurements on nearly the same dates show a

TABLE V

D/H values and measurement techniques. The majority of these methods utilize deuterated molecules for the D/H measurement.

Location	D/H value	Method	Spectral range	Reference
Solar wind	2×10^{-5}	He^3	*in situ* (solar wind)	a
Earth	1.6×10^{-4}	Standard mean ocean water (SMOW)	*in situ*	b
Interstellar medium (ISM)	2×10^{-5}	Absorption of stellar D and H Ly-α lines in the ISM	1216 Å	c
Interstellar clouds	$>10^{-4}$	HCO^+, HCN, H_2O	Thermal radio emission	b
Meteorites	1.6×10^{-4}	Hydrated silicates and organic material	*in situ*	b
Venus	2×10^{-2}	Pioneer Venus	*in situ*	d
		LNMS HDO	2.3 μm	e
Mars	9×10^{-4}	HDO	3.7 μm	f
Jupiter	2×10^{-5}	CH_3D	1.55–1.95 μm	g, h, n , r, s
		HD, Galileo probe	6063.88 Å, 56 μm, *in situ*	
Saturn	2×10^{-5}	CH_3D, HD	1.55–1.95 μm	i, n, o
			56 μm	
Uranus	9×10^{-5}	CH_3D	1.55–1.95 μm	j, u
	5.5×10^{-5}	HD	56 μm	
Neptune	1.2×10^{-4}	CH_3D	1.55–1.95 μm	k, u
	6.5×10^{-5}	HD	56 μm	
Titan	1.6×10^{-4}	CH_3D	1.55–1.95 μm	l, p, q, t
	1×10^{-4}		8.7 μm	
Halley	2×10^{-4}	HDO (Giotto NMS)	*in situ*	m

Note. (a) Geiss and Reeves, 1972, (b) Geiss and Reeves, 1981, (c) McCullough, 1992, (d) Donahue *et al*., 1982, (e) de Bergh *et al*., 1991, (f) Owen *et al*., 1988, (g) Beer and Taylor, 1978, (h) Smith *et al*., 1989, (i) Fink and Larson, 1978, (j) de Bergh, *et al*., 1986, (k) de Bergh, *et al*., 1990, (l) de Bergh *et al*., 1988, (m) Eberhardt, *et al*., 1987, (n) Encrenaz *et al*., 1999, (o) Griffin *et al*., 1996, (p) Orton, 1992, (q) Coustenis *et al*., 2000, (r) Mahaffy *et al*., 1998, (s) Lellouch *et al*., 1997, (t) Taylor and Coustenis, 1998, (u) Feuchtgruber *et al*., 1999.

descrepancy of a factor of 2 (McGrath and Clarke, 1992). They note that this discrepancy may be due to an incorrect value for the interplanetary hydrogen density. These discrepancies, along with the limited Hubble Space Telescope (HST) time dedicated to Saturn in the UV, make the observations of D/H at Saturn and Titan an important goal for the Cassini UVIS.

The first observations of the D/H ratio of Titan showed values considerably higher than those of Saturn (Table VI). Immediately, the question arose how

TABLE VI
Measured and corrected D/H for Titan

	de Bergh *et al.* (1986)	Coustenis *et al.* (1989)	Orton (1992)
Observed D/H [10^{-5}]	$11.1 \leq \text{D/H} \leq 32.6$	$10.0 \leq \text{D/H} \leq 30.0$	$5.50 \leq \text{D/H} \leq 10.0$
Corrected D/H [10^{-5}]	$4.0 \leq \text{D/H} \leq 19.5$	$3.2 \leq \text{D/H} \leq 18.7$	$2.5 \leq \text{D/H} \leq 5.9$

the enrichment in the moon's atmosphere relative to that of Saturn itself could be explained. The early values were close to the SMOW value of 1.56×10^{-4} (Hagemann *et al.*, 1970). A popular scenario was to form the atmosphere of Titan and the earth by in-falling comets (Zahnle and Dones, 1992; Griffith and Zahnle, 1995; Owen and Bar-Nun, 1995, 1996). The most recent determination of the D/H ratio (relating to H_2O) of comet Halley (Eberhardt and Krankowsky, 1995) and the observations of comets Hyakutake (Bocklée-Morvan *et al.*, 1998) and Hale-Bopp (Meier *et al.*, 1998) yield consistent D/H ratios around 30×10^{-5}, well above the SMOW value. Cometary ices could have contributed to the atmosphere, but obviously neither the earth's ocean nor Titan's atmosphere reflect the deuterium enrichment of the cometary icy grains.

Values were derived from ground-based, near-IR observation (de Bergh *et al.*, 1986) of the deuterated methane from the Voyager spacecraft (Coustenis *et al.*, 1989) and by observations in the middle (thermal) infrared (see Orton, 1992). Pinto *et al.* (1986) calculated the enrichment factor over the lifetime of Titan to be between 1.7 and 2.2. Titan's history and formation are quite different from that of the giant planets. Titan was formed from the ices of the early Saturnian nebula. It could not retain molecular hydrogen, and fractionation by atmospheric-loss processes is strong.

It is interesting to note that the most precise determination of the original D/H ratio agrees within the error margin with the proto-solar value, and it cannot be ruled out that there is no (or very little) deuterium enrichment in Titan. It is obvious that a precise determination of the D/H ratio is of high interest and could be a major clue to the formation and history of Titan and of the whole Saturnian system.

7.2. HDAC Usage at Titan

There are two methods for probing the Titan deuterium and hydrogen line profiles during a Titan flyby: (1) modulating the cell optical depth when Titan fills the HDAC field of view, and (2) measuring the HDAC count rate during the Doppler shifts caused by the relative motion between the Cassini orbiter and Titan. During a Titan flyby, the spacecraft Doppler velocity shifts the Lyman-α lines through the absorption profile of the cell. This Doppler effect allows the HDAC to probe the line in wavelength (while simultaneously probing it at different optical depth settings) as the spacecraft flies by Titan. Flybys with the furthest flyby altitudes (less than

90,000 km, the point at which Titan begins to fill the HDAC field of view), are best for HDAC observations because these flybys allow the spacecraft to spend more time near 0 km/s Doppler velocity (where the HDAC absorbs most efficiently).

7.3. Lyman-α Observations at Saturn

All measurements of HDAC include observations of the normal atomic hydrogen, either in photometer mode where the total brightness is registered, or with the absorption switched on when the Lyman-α emission line profile is scanned. Both the variation of the optical depth within the cell or the change in radial velocity component relative to the emitting atoms (or a combination of both methods) will yield information on the emission-line profiles and hence on the temperature and velocity distribution of the hydrogen atoms in the Saturn upper atmosphere.

7.4. Interplanetary/Interstellar Hydrogen

The solar system is moving through interstellar gas at about 20 km s^{-1}, and neutral hydrogen sweeps through the planetary system as interstellar wind. The sun ionizes hydrogen atoms by its EUV radiation and by charge-exchange with the solar wind. The solar emission in the resonance line at Lyman-α exerts a strong radiation pressure force that approximately balances solar gravity. The flow of hydrogen atoms causes an asymmetry of the (interstellar) hydrogen atom density and distribution in the inner planetary system. Lyman-α observations show that the strongest contributions upstream come from a distance of about 5 AU, while downstream the cavity extends to about 20 AU. The variation of solar-wind flux and speed with heliocentric latitude studied in detail by SOHO (Bertaux *et al*., 1997) leads to deviation from the cylinder symmetry. These effects can be most easily observed at a distance of about 10 AU, the heliocentric distance of Saturn (Lallement *et al*., 1995).

The density and velocity distribution (temperature) of interstellar hydrogen are influenced by the interaction with the Sun and its radiation. The solar wind expands into the interstellar plasma until its pressure is balanced by the plasma pressure and interstellar magnetic field defining the heliospheric boundary at around 200 AU. When the interstellar protons try to cross this boundary, they are slowed down, compressed in their density, and heated at the same time (Wallis and Ong, 1975). These processes influence the velocity and density distribution of the hydrogen atoms passing through the inner solar system.

Observations of interplanetary Lyman-α emission have two goals: (1) to determine the physical parameters of the interstellar hydrogen, such as its density, flow velocity, and temperature, and (2) to learn about the properties of the solar wind, such as its latitudinal dependence of its flux and speed, as well as its EUV emission. Elaborate models of the interaction predict the brightness distribution

of interplanetary Lyman-α as a function of the looking direction and position of the observer. A multitude of parameters and their variation with solar cycle can be derived if the observational set is extensive enough. A recent example is provided by the UV spectrometer onboard the Galileo spacecraft (Ajello *et al.*, 1994).

The HDAC can take advantage of a common spacecraft mode in which the Cassini spacecraft slowly rotates during cruise and at Saturn during periods when data are transmitted to earth. These observations will map the Lyman-α brightness consistently over many years. In addition, the absorption of the hydrogen cell can be used to scan through the emission-line profile whenever the radial velocity component of the atoms along the line of sight relative to the Cassini spacecraft is near zero.

7.5. Summary

Information about the D/H and hydrogen line shapes will be extracted from a collection of HDAC count rates at the various optical depths, Doppler velocities, and viewing geometries. These results will provide a comparison to the infrared measurements from ISO and SIRTF for Titan, a key piece of information for theories of the origin and evolution of the Saturn system, the Saturn Lyman-α line shape, and the emissions from the local interstellar medium. Long-term observations and appropriate modeling will allow us to determine the Lyman-α background signal with good accuracy. This is essential in order to measure the foreground contributions of features within the Saturnian system (e.g., Titan's exosphere and torus) with confidence.

8. UVIS Ring Observations

Planetary rings, which just two decades ago were thought unique to the planet Saturn, have now been observed around all the giant planets (for a recent review, see Esposito, 1993). These rings are composed of many particles with a broad range in size. The observed rings systems are quite diverse. Jupiter's ring is optically thin and composed of dustlike small particles (Showalter *et al.*, 1987). Saturn's rings are broad, bright, and opaque (Cuzzi *et al.*, 1984; Esposito *et al.*, 1984). Uranus has narrow, dark rings among broad lanes of dust that are invisible from Earth (French *et al.*, 1991; Esposito *et al.*, 1991). Neptune's rings include incomplete arcs restricted to a small range of the circumference (Porco *et al.*, 1995). All rings lie predominantly within their planet's Roche limit, where tidal forces would destroy a self-gravitating body (Nicholson and Dones, 1991). They are also within the planet's magnetosphere, and in the case of Uranus, they are within the upper reaches of the planetary atmosphere. Saturn's rings are the largest of any planet's, and show all the diverse phenomena seen in other ring systems.

8.1. Voyager Results and Cassini Capabilities

Voyager 1 and 2 made the closest investigations of Saturn's rings in 1980 and 1981. These missions provided images, spectra, and radio and stellar occultations as well as information on the ring environment. Reviews are provided by Cuzzi *et al.* (1984) and Esposito *et al.* (1984). The radio occultation, stellar occultation, and sequences of images each provided complete radial coverage of the ring system (Figure 25). Conversely, the azimuthal coverage is more sketchy. As to temporal coverage, the data encompass only a few weeks around each encounter, with the best resolution data for each from a period of less than a day. The images are all from the Voyager Reticon cameras: the spectral sensitivity of their silicon detectors explains why we have no pictures in the UV or IR. This information is now supplemented by data from the ground, HST, and IUE, which all lack the radial, azimuthal, and temporal resolution provided briefly by the spacecraft encounters. A new data set from the spectacular 1995 ring-plane crossing (see Nicholson *et al.*, 1996; Showalter, 1997) provides information on the more transparent rings. The thickest parts of Saturn's rings were not penetrated by either the radio or stellar occultations.

The Cassini mission provides the opportunity to measure the rings at high resolution in the radial, azimuthal, and vertical dimensions over a period of 4 years.

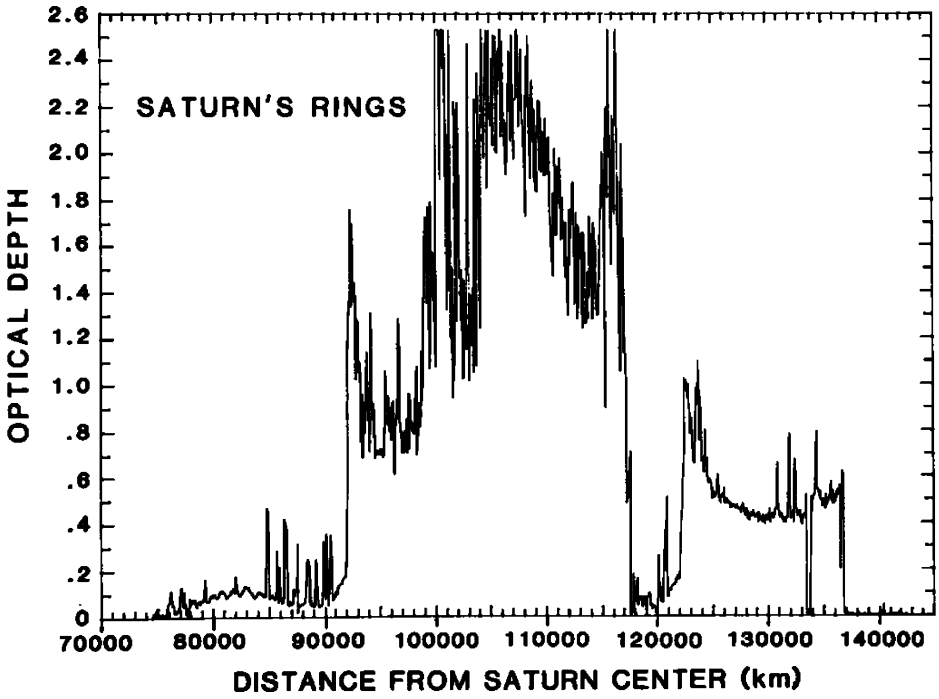

Figure 25. Saturn's rings from the Voyager 2 PPS δ Scorpii stellar occultation showing ring radial structure (Esposito *et al.*, 1983a).

Observations of the ring environment, magnetosphere, and small nearby satellites will determine the interactions of the various parts of the Saturn system with its rings. The UVIS experiment has the capability for imaging, spectroscopy, and high speed photometry that can contribute to these scientific objectives.

8.2. Ring Structure

Figure 26 shows observations of density waves in Saturn's rings from the Voyager PPS occultation (Esposito *et al.*, 1983a,b). These features are but one of a number of dynamic phenomena evident in the ring radial profile. The UVIS High Speed Photometer (HSP) channel has been optimized to follow up on the Voyager investigations. The HSP field of view is 6 mrad × 6 mrad, large enough that no brightness modulations are expected from pointing variations. The CsI photocathode is essentially solar-blind, allowing high signal-to-noise occultations of both sunlit and shadowed rings. The HSP is bore-sighted with the spectroscopic channels, allowing concurrent spectroscopy of the transmitted starlight from 91 to 190 nm. Simultaneously, we can obtain a long slit image

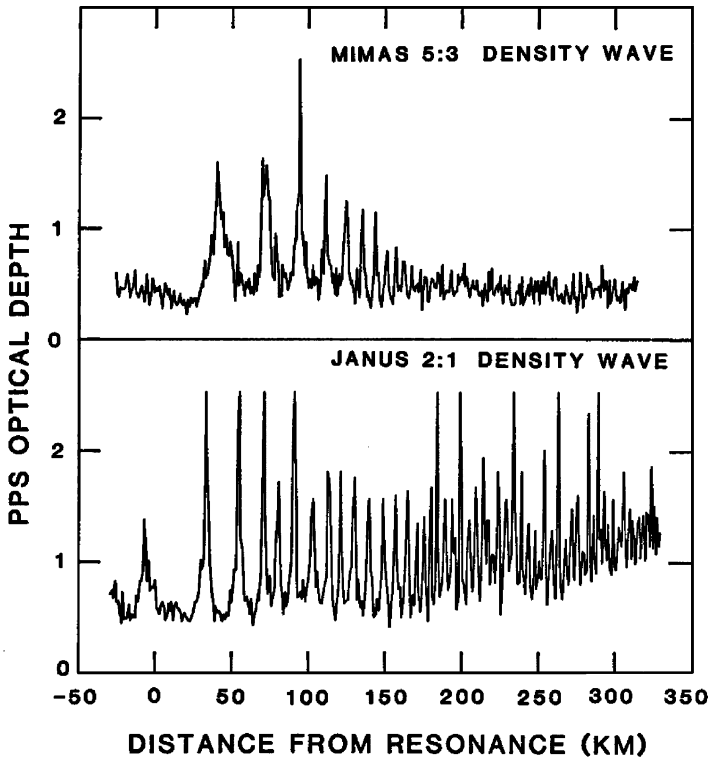

Figure 26. Density waves seen in the PPS occultation (Esposito *et al.*, 1983b). Compare the resolution with Figure 25.

of the occultation point up to a distance ±30 mrad, allowing the observation of diffracted light in the stellar aureole. The time resolution of 2 ms can give spatial resolution of 20 m or better on the rings, comparable to the diffraction limit.

The large mirror and amplifiers in the HSP allow very high counting rates. We expect 2000 counts in 2 ms for the occultation star δ Sco. This compares to the Voyager PPS observation of δ Sco of 39 counts every 10 ms (Esposito *et al*., 1983a). Thus the Cassini UVIS HSP can probe structures five times narrower than Voyager, with 50 times the signal in each integration period. This high sensitivity and resolution will be used to probe wakes, waves, and ring edges.

Occultation tracks at multiple ring longitudes will likely reveal azimuthal asymmetries in the rings, as was seen by the Voyager PPS at Uranus (Colwell *et al*., 1990) and ground-based stellar occultation observations of Neptune's rings (Elliot *et al*., 1985; Covault *et al*., 1986; French *et al*., 1993). These asymmetries may provide clues to the origin of the ring features and imply the presence of nearby perturbing satellites. These data will be used to constrain physical models of their origin and evolution.

Radial optical depth profiles will be generated from stellar occultation measurements (Colwell and Esposito, 1990a,b). Accurate absolute determinations of the locations of edges, gaps, and wave features in the data will allow the identification of new ring-satellite resonances, and quite possibly the indirect detection of new, small satellites within the ring system (e.g., Horn *et al*., 1990). Such satellites are linked to the evolution and the origin of the rings. Their number and distribution within the rings will help constrain theories of ring origin (Colwell, 1994; Sicardy and Lissauer, 1992).

During HSP observations of stellar occultations, the UVIS Far Ultraviolet channel (FUV) will measure ring background brightness. These measurements will also provide information on the size distribution of small (micrometer-sized) dust particles in the rings during occultations by the shadowed rings. Dust in Saturn's rings will produce a diffraction aureole detectable by the FUV channel of UVIS. This diffraction signature is sensitive to the characteristic dust particle size. Size distributions based on different physical models of the creation, transport, and destruction of dust will be tested against the observations. The abundance, size, and distribution of dust in the rings are useful diagnostics for the size distribution, velocity distribution, and surface properties of the larger ring particles, which act as sources and sinks of dust in the rings (Colwell and Esposito, 1990a,b). Data on these larger particles will be obtained from stellar occultations and combining UVIS reflectance data with images from the Cassini Imaging Science Subsystem (ISS) and Visual and Infrared Mapping Spectrometer (VIMS). The FUV data will also be used to determine the magnitude of the ring background signal to be removed from the HSP occultation data. Figures 27 and 28 show the multitude of available opportunities and the progress of a stellar occultation from Cassini tour T18-5.

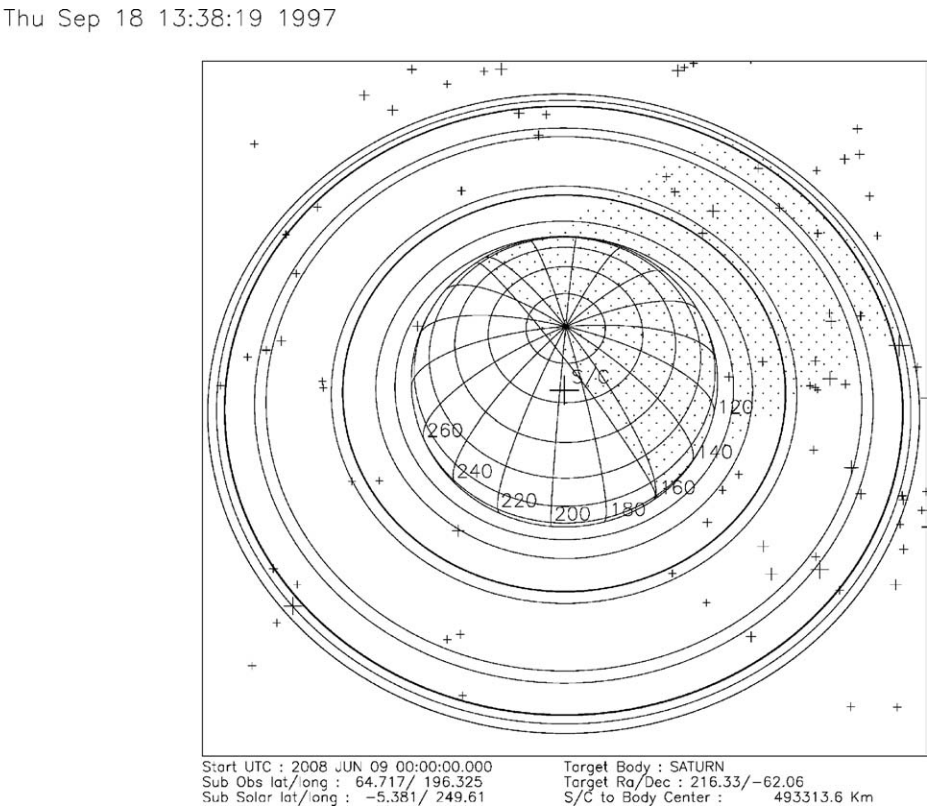

Figure 27. Numerous ring stellar occultation opportunities are shown with CASPER (Cassini Sequence Planner) software in this near-polar view of Saturn and its ring system. Plus symbols indicate stars; larger symbols are brighter stars. The stippled region indicates Saturn's shadow. The subspacecraft point is indicated by a cross on the planet.

8.3. UVIS IMAGES

During remote-sensing ring observations, UVIS will slew its slit to make images of the rings. At a range of 10^6 km, the UVIS resolution of 1 mrad gives a picture element of 1000 km width. Typical images will be 64 elements tall (along the slit), with the image width determined by the total slew duration. Because UVIS has the shortest wavelength of any of the remote sensing instruments, it will be more sensitive to the smallest particles in the rings, with sizes as small as 0.01 to 0.1μ. The images at different UV wavelengths can be compared to camera images to determine the dust contribution and extend the size distribution. The ring 'spokes' are one natural target. By combining the UV observations with CIRS spectra, ISS, VIMS images, and radio occultations, the size distribution of the ring particles can be measured from submicron to meter sizes.

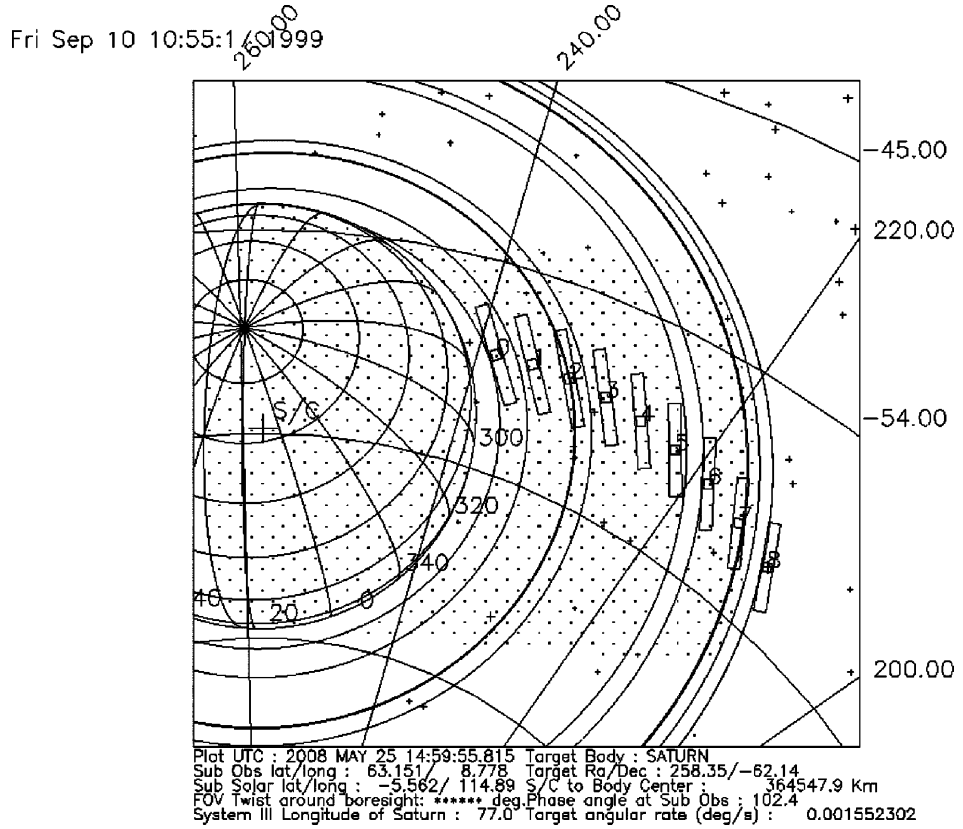

Figure 28. The star β Cen is occulted by the shadowed rings of Saturn. The FUV occultation slit and the HSP aperture are shown around the star.

8.4. Ring Composition

The reflectance spectrum of Saturn's rings from IUE and Voyager clearly shows the water absorption edge at 1650 Å. We will map the depth and wavelength of this feature across the rings to determine compositional and age variations. At wavelengths of 1800 to 2000 Å, water ice is transparent, and the non-icy ring component may be studied.

During systematic spectroscopy of the Saturn system, UVIS will map the emissions from neutral hydrogen (1216 Å) and oxygen (1304 Å and 1356 Å). Emissions near the rings will define the ring atmosphere (Broadfoot *et al.*, 1981; Hall, 1996) and the interactions of the ring with its local environment. This will constrain the long-term evolution of the ring particles. UVIS will also measure remotely a number of magnetospheric constituents (particularly H, O, N, and D) that will define the broader ring-magnetosphere interactions.

8.5. Ring History

The UVIS and the other remote-sensing and *in situ* Cassini experiments will provide a rich data set on the current state of the rings and their present interactions with other parts of the Saturn system.

A comprehensive model of the origin and large-scale evolution of Saturn's rings will be developed based on the ensemble of Cassini observations at Saturn. Crater statistics on the larger satellites and the anticipated discovery of smaller ring moons will allow development of an accurate model of the time-dependent interplanetary impacting flux at intermediate and large sizes. This flux, when combined with theoretical and experimental results on catastrophic fragmentation, drives the global evolution of the ring system. Disruption of satellites or 'rubble piles' creates new ring particles. These then undergo orbital evolution, influenced by gravitational perturbations from other satellites, and partial accretion (Canup and Esposito, 1995). Dust is produced within the ring from interparticle collisions and micrometeoroid bombardment. These processes can be combined into a single global Markov chain simulation of the ring system (Colwell and Esposito, 1993) for time scales of the age of the solar system. Monte Carlo simulations can be conducted using the same transition probabilities in order to create simulated histories of the rings system for direct comparison with Cassini observations.

Variations of the abundance of dust between different ring features will provide additional information on ring particle characteristics, including collision velocities and regolith properties. Dynamically active regions may exhibit different dust abundances than quiescent regions in the rings. Features such as arcs, kinks, braids, and other azimuthal asymmetries may indicate a mode of origin from satellite disruption or complex gravitational interactions with nearby satellites. The distribution of small moons, their resonances, and density waves and gaps within the rings will be used to characterize the large-scale transport of angular momentum through the system for use in global evolution models of the rings.

8.6. Summary

The UVIS ring studies will provide (1) a comprehensive study of features in Saturn's rings, including their dynamical links to embedded satellites, (2) a determination of the abundance and size distribution of dust within the rings as a function of location within the rings, (3) modeling of ring processes and system interactions at short time scales, and (8) models of the global evolution of the rings over the age of the solar system.

9. Conclusions

The UVIS investigation aboard the Cassini orbiter will provide key new information on the chemistry of the Titan and Saturn atmospheres; their clouds and aerosols;

exospheres, thermospheres, and magnetospheres in the Saturn system; satellite surfaces and atmospheres; Titan's atomic D/H ratio; and the physics and history of rings. These results are enabled by the spectroscopic and imaging capabilities of UVIS, the long-time coverage allowed by the Cassini orbit, stellar and solar occultations, multiple phase angles, close-up maps, limb scans, and synergistic investigations with other Cassini experiments.

Acknowledgement

This work was supported by the National Aeronautics and Space Administration under JPL Contract 961196. The Hydrogen Deuterium Absorption Cell (HDAC) was designed and constructed with support from the Max-Planck-Gesellschaft zur Foerderung der Wissenschaften. Grants were received from the DLR under FKZ 50 OH 9201 7. The authors thank Sushil Atreya and an anonymous reviewer for their helpful comments.

References

Ajello, J. M., Pryor, W. R., Barth, C. A., Hord, C. W., Stewart, A. I. F., Simmons, K. E., *et al.*: 1994, *Astron. Astrophys.* **289**, 283.

Atreya, S. K.: 1982, *Plan. Space Sci*. **30**, 849.

Atreya, S. K., Donahue, T. M., and Kuhn, W. R.: 1978, *Science* **201**, 611.

Atreya, S. K., Waite, J. H., Jr., Donahue, T. M., Nagy, A. F., and McConnell, J. C.: 1988, 'Theory, measurements, and models of the upper atmosphere and ionosphere of Saturn', in Gehrels, T. and Matthews, M. S. (eds.), *Saturn*, University of Arizona Press, Tucson, p. 239.

Atreya, S. K., Wong, M. H., Owen, T. C., Mahaffy, P. R., Niemann, H. B., de Pater, I., *et al.*: 1999, *Planet. Space Sci*. **47**, 1243.

Babichenko, S. I., Deregusov, E. V., Kurt, V. G., Romanova, N. N., Skljankin, V. A., Smirnov, A. S., *et al.*: 1977, *Space Sci. Instr.* **3**, 271.

Baragiola, R. A. and Bahr, D. A.: 1998, *J. Geophys. Res*. **103**, 25865.

Bar-Nun, A., Kleinfeld, I., and Ganor, E.: 1988*, J. Geophys. Res. (Atmospheres*) **93**, 8383.

Barth, C. A., Hord, C. W., Stewart, A. I. F., Pryor, W. R., Simmons, K. E., McClintock, W. E., Ajello, J. M., Naviaux, K. L., and Aiello, J. J.: 1997, *Geophys. Res. Lett.* **24**, 2147.

Bertaux, J. L.: 1977, *Nature* **270**, 156.

Bertaux, J. L.: 1978, *Planet. Space Sci.* **26**, 431.

Bertaux, J. L., Blamont, J. E., Lepine, V. M., Kurt, V. G., Romanova, N. N., and Smirnov, A. S.: 1978, *Planet. Space Sci.* **26**, 817.

Bertaux, J. L., Goutail, F., Dimarellis, E., Kockarts, G., and Van Ransbeeck, E.: 1984, *Nature* **309**, 771.

Bertaux, J. L., Quémerais, E., Lallement, R., Kyrölä, E., Schmidt, W., Summanen, T., Goutail, J. P., *et al.*: 1997, *Solar Phys.* **175**, 737.

Bockelée-Morvan, D., Gautier, D., Lis, D. C., Young, K., Keene, J., Phillips, T. G., *et al.*: 1998, *Icarus* **133**, 147.

Broadfoot, A. L., Belton, M. J. S., Takacs, P. Z., Sandel, B. R., Shemansky, D. E., Holberg, J. B., *et al.*: 1979, *Science* **204**, 979.

Broadfoot, A. L., Sandel, B. R., Shemansky, D. E., Holberg, J. B., Smith, G. R., Strobel, D. F., *et al.*: 1981, *Science* **212**, 206.

Buratti, B. J.: 1988, *Icarus* **75**, 113.

Buratti, B. and Veverka, J.: 1984, *Icarus* **58**, 254.
Cabane, M., Rannou, P., Chassefiere, E., and Israel, G.: 1993, *Planet. Space Sci.* **41**, 257.
Calvin, W. M., Johnson, R. E., and Spencer, J. R.: 1996, *Geophys. Res. Lett*. **23**, 673.
Canup, R. M. and Esposito, L. W.: 1995, *Icarus* **113**, 331.
Chassefiere, E. and Cabane, M.: 1995, *Planet. Space Sci.* **43**, 91.
Cheng, A. F., Haff, P. K., Johnson, R. E., and Lanzerotti, L. J.: 1986, 'Interactions of planetary magnetospheres with icy satellite surfaces', in Burns, J. A., and Matthews, M. S. (eds.), *Satellites*, University of Arizona Press, Tucson, p. 403.
Clark, R. N., Brown, R. H., Owensby, P. D., and Steele, A.: 1984, *Icarus* **58**, 265.
Clark, R. N., Fanale, F. P., and Gaffey, M. J.: 1986, 'Surface composition of natural satellites', in Burns, J. A., and Matthews, M. S. (eds.), *Satellites*, Univ. Ariz. Press, Tucson, p. 437.
Clarke, D. W. and Ferris, J. P.: 1997,*Icarus* **127**, 158.
Colwell, J. E.: 1994, *Planet. Space Sci*. **42**, 1139.
Colwell, J. E. and Esposito, L. W.: 1990a, *Icarus* **86**, 530.
Colwell, J. E. and Esposito, L. W.: 1990b, *J. Geophys. Res.* **17**, 1741.
Colwell, J. E. and Esposito, L. W.: 1993, *J. Geophys. Res. (Planets)* **98**, 7387.
Colwell, J. E., Horn, L. J., Lane, A. L., Esposito, L. W., Yanamandra-Fisher, P. A., Pilorz, S. H., *et al.*: 1990, *Icarus* **83**, 102.
Coustenis, A.: 1992, 'Titan's atmosphere: Latitudinal variations in temperature and composition', in *Symposium on Titan*, Conf. Proc. ESA, SP 338, 53.
Coustenis, A., and Bezard, B.: 1995, *Icarus* **115**, 126.
Coustenis, A., Bezard, B., and Gautier, D.: 1989, *Icarus* **80**, 54.
Coustenis, A., Bezard, B., Gautier, D., Marten, A., and Samuelson, R.: 1991, *Icarus* **89**, 152.
Covault, C. E., Glass, I. S., French, R. G., and Elliot, J. L.: 1986, *Icarus* **67**, 126.
Cravens, T. E., Howell, E., Waite, J. H., and Gladstone, G. R.: 1995, *J. Geophys. Res.* **100**, 17153.
Cuzzi, J. N., Lissauer, J. J., Esposito, L. W., Holberg, J. B., Marouf, E. A., Tyler, G. L., *et al.*: 1984, 'Saturn's rings: Properties and processes', in Greenberg, R. and Brahic, A. (eds.), *Planetary Rings*, University of Arizona Press, Tucson, p. 73.
de Bergh, C., Bézard, B., Owen, T., Crisp, D., Maillard, J. P., and Lutz, B. L.: 1991, *Science* **251**, 547.
de Bergh, C., Lutz, B. L., Owen, T., Brault, J., and Chauville, J.: 1986, *Astrophys. J.* **311**, 501.
de Bergh, C., Lutz, B. L., Owen, T., and Chauville, J.: 1988, *Astrophys. J.* **329**, 951.
de Bergh, C., Lutz, B. L., Owen, T., and Maillard, J. P.: 1990, *Astrophys. J.* **355**, 661.
Degraauw, T., Feuchtgruber, H., Bezard, B., Drossart, P., and Encrenaz, T.: 1997, *Astron. Astrophys*. **321**, L-13.
Delitsy, M. L., and Lane, A. L.: 1998, *J Geophys. Res.* **103**, 31391.
Dessler, A. J.: 1981, *Planet. Space Sci.* **29**, 215.
Devanssay, E., Gazeau, M. C., Guillemin, J. C., and Raulin, F.: 1995, *Planet. Space Sci*. **43**, 25.
Donahue, T. M., Hoffman, J. H., Hodges, R. R., Jr., and Watson, A. J.: 1982, *Science* **216**, 712.
Eberhardt, P., Dolder, U., Schutte, W., Krankowsky, D., Lammerzahl, P., Hoffman, J. H., *et al.*: 1987, *Astron. Astrophys*. **187**, 435.
Eberhardt, P., and Krankowsky, D.: 1995, *Astron. Astrophys.* **295**, 795.
Elliot, J. L., Baron, R. L., Dunham, E. D., French, R. G., and Meech, K. J.: 1985, *Astron. J*. **90**, 2615.
Encrenaz, T., Drossart, P., Feuchtgruber, H., Lellouch, E., Bézard, B., Fouchet, T., *et al.*: 1999, *Planet. Space Sci.* **47**, 1223–1240.
Esposito, L. W.: 1993, *Ann. Rev. Earth Planet. Sci*. **21**, 487.
Esposito, L. W., Brahic, A., Burns, J. A., and Marouf, E. A.: 1991, 'Particle properties and processes in uranus' rings', in Bergstralh, J. T., Miner, E. D., and Matthews, M. S. (eds.), *Uranus*, University of Arizona Press, Tucson, p. 410.

Esposito, L. W., Cuzzi, J. N., Holberg, J. B., Marouf, E. A., Tyler, G. L., and Porco, C. C.: 1984, 'Saturn's rings: Structure, dynamics and particle properties', in Gehrels, T. and Matthews, M. S. (eds.), *Saturn,* University of Arizona Press, Tucson, p. 463.

Esposito, L. W., O'Callaghan, M., Simmons, K. E., Hord, C. W., West, R. A., Lane, A. L., *et al.*: 1983a, *J. Geophys. Res*. **88**, 8643.

Esposito, L. W., O'Callaghan, M., and West, R. A.: 1983b, *Icarus* **56**, 439.

Feldman, P. D., McGrath, M. A., Moos, H. W., Durrance, S. T., Strobel, D. F., and Davidsen, A. F.: 1993, *Astrophys. J.*, **406**, 279.

Festou, M. C. and Atreya, S. K.: 1982, *Geophys. Res. Lett*. **9**, 1147.

Feuchtgruber, H., Lellouch, E., Bézard, B., Encrenaz, T., deGraauw, T., and Davis, G.: 1999, *Astron. Astrophys.* **341**, L17–L21.

Fink, U. and Larson, H. P.: 1978, *Science* **201**, 343.

French, R. G., Maeue, S., Mason, E. C., McGhee, C. A., Nicholson, P. D., Matthews, K., and Roques, F.: 1993, *Bull. Amer. Astron. Soc.* **25**, 1110.

French, R. G., Nicholson, P. D., Porco, C. C., and Marouf, E. A.: 1991, 'Dynamics and structure of the uranian rings', in Bergstralh, J. T., Miner, E. D., and Matthews, M. S. (eds.), *Uranus*, University of Arizona Press, Tucson, p. 327.

Geiss, J. and Reeves, H.: 1972, *Astron. Astrophys*. **18**, 126.

Geiss, J. and Reeves, H.: 1981, *Astron. Astrophys.* **93**, 189.

Gladstone, G. R., Allen, M., and Yung, Y. L.: 1996, *Icarus* **119**, 1.

Gladstone, G. R., Waite, J. H., and Lewis, W. S.: 1998, *J. Geophys. Res.* **103**, 20083.

Griffin, M. J., Naylor, D. A., Davis, G. R., Ade, P. A. R., Oldham, P. G., Swinyard, B. M., *et al.*: 1996, *Astron. Astrophys.* **315**, L389–L392.

Griffith, C. A. and Zahnle, K. Z.: 1995., *J. Geophys. Res.* **100**, 16,907.

Gurwell, M. A. and Muhleman, D. O.: 1995, *Icarus* **117**, 375.

Hagemann, R., Nief, G., and Roth, E.: 1970, *Tellus* **22**, 712.

Hall, D. T.: 1996, *Science* **272**, 516.

Hall, D. T., Shemansky, D. E. and Tripp, T. M.: 1992, 'A reanalysis of Voyager UVS observations of Titan', in *Symposium on Titan*, Conf. Proc. ESA, SP-338, p. 69.

Hall, D. T., Strobel, D. F., Feldmann, P. D., McGrath, M. A. and Weaver, H. A.: 1995, *Nature* **373**, 677.

Hendrix, A. R., Barth, C. A., and Hord, C. W.: 1999, *J. Geophys. Res. (Planets)* **104**, 14169.

Hendrix, A. R., Barth, C. A., Hord, C. W., and Lane, A. L.: 1998,*Icarus* **135**, 79.

Hidayat, T., Marten, A., Bezard, B., Gautier, D., Owen, T., Matthews, H. E., *et al.*: 1997, *Icarus* **126**, 170.

Horn, L. J., Yanamandra-Fisher, P. A., and Esposito, L. W.: 1990, *Icarus* **76**, 485.

Jaffel, L. B., V'eronique, L., and Sandel, B. R.: 1995, *Science* **269**, 951.

Johnson, R. E.: 1997, *Icarus* **128**, 469.

Johnson, R. E., and Quickenden, T. I.: 1997, *J. Geophys. Res. (Planets)* **102**, 10985.

Karkoschka, E., and Lorenz, R. D.: 1997, *Icarus* **125**, 369.

Kawahara, T.: 1994, 'A Study on Hydrogen/Deuterium Absorption Cell Technique for Spacecraft Observations of Planetary Atmospheres', Ph.D. dissertation, Tohoku University, Japan.

Kawahara, T., Okano, S., Abe, T., and Fukunishi, H.: 1993, *Tohoku Geophys. J. Sci. Rep.*, ser. 51, **34**, 35.

Khare, B. N., Sagan, C., Arakawa, E. T., Suits, F., Callcott, T. A., and Williams, M. W.: 1984, *Icarus* **60**, 127.

Kivelson, M. G., Warnecke, J., Bennett, L., Joy, S., Khurana, K. K., Linker, J. A., *et al.*: 1997, *J. Geophys. Res. (Planets)* **103**, 19963.

Lallement, R., Kyroelae, E., and Summanen, T.: 1995, *Space Sci. Rev.* **72**, 455.

Lane, A. L., Hord, C. W., West, R. A., Esposito, L. W., Coffeen, D. L., Sato, M., *et al.*: 1982, *Science* **215**, 537.

Lara, L. M., Lellouch, E., Lopezmoreno, J. J., and Rodrigo, R.: 1996, *J. Geophys. Res*. **101**, 23261.
Lawrence, G. M. and McClintock, W. E.: 1996, *Proc. SPIE* **2831**, 104.
Lellouch, E., Feuchtgruber, H., de Graauw, T., Encrenaz, T., Bézard, B., and Griffin, M.: 1997, 'Deuterium and oxygen in the giant planets', in Kessler, M (ed.), *Proceedings of the First ISO Workshop on Analytical Spectroscopy*, ESA SP-419, Madrid, 6–8 October, p. 131.
Lemmon, M. T.: 1994, Ph.D. dissertation, University of Arizona, Tucson.
Lunine J. I. and Stevenson, D. J.: 1985, *Astrophys. J. Supp. Ser.* **58**, 493.
Lutz, B. L., de Bergh, C., and Owen, T.: 1983, *Icarus* **220**, 1274.
Mahaffy, P. R., Donahue, T. M., Atreya, S. K., Owen, T. C., and Niemann, H. B.: 1998, *Space Sci. Rev*. **84**, 251.
Maki, J. N.: 1996, 'The hydrogen deuterium absorption cell on the sCassini spacecraft: A remote sensing instrument for atomic D/H measurements on Saturn and Titan', Ph.D. dissertation, University of Colorado, Boulder.
Marten, A., Gautier, D., Tanguy, L., Lecacheux, A., Rosolen, C., and Paubert, G.: 1988, *Icarus* **76**, 558.
McClintock, W. E., Lawrence, G. M., Kohnert, R. A., and Esposito, L. W.: 1992, *Proc. SPIE* **1745**, 26.
McClintock, W. E., Lawrence, G. M., Kohnert, R. A., and Esposito, L. W: 1993, *Opt. Eng.* **32**, 3038.
McCullough, P.: 1992, *Astrophys. J.* **390**, 213.
McGrath, M. and Clarke, J. T.: 1992, *J. Geophys. Res.* **97** (A9), 13691.
McGrath, M. A., Courtin, R., Smith, T. E., Feldman, P. D., and Strobel, D. F.: 1998, *Icarus* **131**, 382.
McKay, C. P.: 1996, *Planet. Space Sci.* **44**, 741.
Meier, R., Owen, T. C., Matthews, H. E., Jewitt, D. C., Bockelée-Morvan, D., Biver, N., *et al.*: 1998, *Science* **279**, 842.
Morton, D., and Purcell, J.: 1961, 'Rocket Observations of Lyman-α in the Night Sky', *Report of NRL Progress*, June 1961.
Moses, J. I., Bezard, B., Lellouch, E., Gladstone, G. R., Feuchtgruber, H., and Allen, M.: 2000, *Icarus* **143**, 244.
Muhleman, D. O., Berge, G. L., and Clancy, R. T.: 1984, *Science* **223**, 393.
Nelson, R. M., and Lane, A. L.: 1987, 'Planetary satellites', in Kondo, Y. (ed.), *Scientific Accomplishments of the IUE*, p. 67.
Nicholson, P. D., and Dones, L.: 1991, *Rev. Geophys*. **29**, 313.
Nicholson, P. D., Showalter, M. R., Dones, L., French, R. G., Larson, S. M., Lissauer, J. J., *et al.*: 1996, *Science* **272**, 509.
Noll, K. S., Geballe, T. R., Knacke, R. F., and Pendleton, Y. J.: 1996a, *Icarus* **124**, 625.
Noll, K. S., Johnson, R. E., Lane, A. L., Dominque, D. L., and Weaver, H. A.: 1996b, *Science* **273**, 341.
Noll, K. S., Roush, T. L., Cruikshank, D. P., Johnson, R. E., and Pendleton, Y. J.: 1997, *Nature* **388**, 45.
Orton, G.: 1992, 'Ground-based observations of Titan's thermal spectrum', in *Symposium on Titan*, Conf. Proc. ESA, SP-338, 81.
Orton, G. L., Serabyn, E., and Lee, Y. T.: 2000, *Icarus* **146**, 48–59.
Owen, T.: 1994, *Astrophys. Space Sci.* **212**, 1.
Owen, T. and Bar-Nun, A.: 1995, *Icarus* **116**, 215.
Owen, T. and Bar-Nun, A.: 1996, *Earth, Moon, Planets* **72,** 425.
Owen, T., Lutz, B. L., and de Bergh, C.: 1986, *Nature* **320**, 245.
Owen, T., Mahaffy, P., Niemann, H. B., Atreya, S., Donahue, T., Bar-Nun, A., *et al.*: 1999, *Nature* **402**, 269.
Owen, T., Maillard, J., de Bergh, C., and Lutz, B.: 1988, *Science* **240**, 1767.
Pinto, J. P., Lunine, J. I., Kim, S. J., and Yung, Y. L.: 1986, *Nature* **319**, 388.
Porco, C. C., Cuzzi, J. N., Esposito, L. W., Lissauer, J. J., and Nicholson, P. O.: 1995, 'Neptune's ring system', in Bergstralh, J., Miner, E. D., and Matthews, M. S. (eds.) *Neptune and Triton,* University Arizona Press, Tucson.
Pryor, W. R. and Hord, C. W.: 1991, *Icarus* **91**, 161.

Rages, K. and Pollack, J. B.: 1983, *Icarus* **55**, 50.
Rannou, P., Cabane, M., Botet, R., and Chassefiere, E.: 1997, *J. Geophys. Res*. **102**, 10997.
Sandel, B. R. and Broadfoot, A. L.: 1981, *Nature* **292**, 679.
Sandel, B. R., Shemansky, D. E., Broadfoot, A. L., Holberg, J. B., Smith, G. R., McConnell, J. C., *et al.*: 1982, *Science* **215**, 548.
Saur, J., Strobel, D. F., and Neubauer, F. M.: 1998, *J. Geophys. Res. (Planets)* **103**, 19947.
Scattergood, T. W., Lau, E. Y., and Stone, B. M.: 1992, *Icarus* **99**, 98.
Shemansky, D. E.: 1985, *J. Geophys. Res.* **90**, 2673.
Shemansky, D. E. and Ajello, J. M.: 1983, *J. Geophys. Res.* **88**, 459.
Shemansky, D. E., Kanik, I., and Ajello, J. M.: 1995, *Astrophys. J.* **452**, 480.
Shemansky, D. E., Matheson, P., Hall, D. T., Hu, H. Y., and Tripp, T. M.: 1993, *Nature* **363**, 329.
Showalter, M. R.: 1997, Paper presented at Ring-Plane Crossing Workshop, Wellesley, Massachusetts, abstracted in *Bull. Am. Astron. Soc.* **29**, 999.
Showalter, M. R., Burns, J. A., Cuzzi, J. N., and Pollack, J. B.: 1987, *Icarus* **69**, 458.
Showman, A. P. and Ingersoll, A. P.: 1998, *Icarus* **132**, 205.
Sicardy, B. and Lissauer, J. J.: 1992, *Adv. Space Res.* **12**, 97.
Smith, B. A., Soderblom, L., Batson, R., Bridges, P., Inge, J., Masursky, H., *et al*.: 1982, *Science* **215**, 504.
Smith, G. R. and Hunten, D. M.: 1990, *Rev. Geophys*. **28**, 117.
Smith, G. R., McConnell, J. C., Shemansky, D. E., Holberg, J. B., Broadfoot, A. L., and Sandel, B. R.: 1983, *J. Geophys. Res*. **88**, 8667.
Smith, W. H., Schempp, W. V., and Baines, K.: 1989, *Astrophys. J.* **336**, 967.
Spencer, J. R., Calvin, W. M., and Person, M. J.: 1995*, J. Geophys. Res.* **100**, 19049.
Squyres, S. W., Reynolds, R. T., Cassen, P. M., and Peale, S. J.: 1983, *Icarus* **53**, 319.
Stevenson, D. J.: 1982, *Nature* **298**, 142.
Stevenson, D. J.: 1991, 'Interior of Titan', in *Symposium on Titan,* Conf. Proc. ESA, SP-338, p. 29.
Taylor, F. W. and Coustenis, A.: 1998, *Planet. Space Sci*. **46**, 1085–1097.
Thompson, W. R., McDonald, G. D., and Sagan, C.: 1994, *Icarus* **112**, 376.
Tomasko, M. G. and Smith, P. H.: 1982,*Icarus* **51**, 65.
Toon, O. B., McKay, C. P., Griffith, C. A., and Turco, R. P.: 1992, *Icarus* **95**, 24.
Trauger, J. T., Clarke, J., Bellester, G., Evans, R., Burrows, C., Crisp, D., *et al.*: 1998, *J. Geophys. Res.* **103**, 20237.
Veverka, J. P., Thomas, P., Johnson, T. V., Matson, D., and Housen, K.: 1986, in Burns, J. A., and Matthews, M. S. (eds.), *Satellites,* University of Arizona Press, Tucson, p. 342.
Vidal, R. A., Bahr, D., Baragiola, R. A., and Peters, M.: 1997, *Science* **276**, 1839.
Waite, J. H., Bagenal, F., Seward, F., Na, C., Gladstone, G., Cravens, T., *et al*.: 1994, *J. Geophys. Res.* **99**, 14799.
Wallis, M. K. and Ong, R. S. B.: 1975, *Planet. Space Sci.* **23**, 713.
West, R. A., Friedson, A. J. and Appleby, J. F.: 1992, *Icarus* **100**, 245.
West, R. A. and Smith, P. H.: 1991, *Icarus* **90**, 330.
Winter, T. C. and Chubb, T. A.: 1967, *J. Geophys. Res.* **72**, 4405.
Yelle, R. V., Sandel, B. R., Shemansky, D. E., and Kumar, S.: 1986, *J. Geophys. Res.* **91**, 8756.
Young, L. A., Yelle, R. V., and Young, R. E.: 1998, *Bull. Am. Astron. Soc.* **30**, 1075.
Young, L. A., Yelle, R. V., Young, R., Seiff, A., and Kirk, D. B.: 1997, *Science* **276**, 108.
Yung, Y. L., Allen, M., and Pinto, J. P.: 1984, *Astrophys. J. Supp. Ser.* **55**, 465.
Yung, Y. L. and DeMore, W. B.: 1999, *Photochemistry of Planetary Atmospheres*, Oxford University Press, New York.
Zahnle, K. and Dones, L.: 1992, 'Impact Origin of Titan's Atmosphere', in *Symposium on Titan*, Conf. Proc. ESA, SP-338, 19.
Zwier, T. S. and Allen, M.: 1996, *Icarus* **123**, 578.